

Changes in mesophotic carbonate-platform export across the end of the last glacial cycle (Saya de Malha Bank, western Indian Ocean)

Or M. Bialik^{1,2}  | Christian Betzler³ | Juan Carlos Braga⁴ | John J. G. Reijmer⁵  | Jesus Reolid⁴ | Sebastian Lindhorst³

¹Institute of Geology and Palaeontology, University of Münster, Münster, Germany

²Dr. Moses Strauss Department of Marine Geosciences, The Leon H. Charney School of Marine Sciences, University of Haifa, Carmel, Israel

³Institut für Geologie, Universität Hamburg, Hamburg, Germany

⁴El Departamento de Estratigrafía y Paleontología, Facultad de Ciencias, Avenida de la Fuente Nueva, Granada, Spain

⁵Department of Geosciences, Faculty of Science, Vrije Universiteit Amsterdam, Amsterdam, The Netherlands

Correspondence

Or M. Bialik, Institute of Geology and Palaeontology, University of Münster, Corrensstr. 24, Münster 48149, Germany.

Email: obialik@campus.haifa.ac.il

Funding information

H2020 Marie Skłodowska Curie fellowship, Grant/Award Number: 101003394; Ministerio de Ciencia e Innovación, Grant/Award Number: RYC2021-034362-I; Bundesministerium für Bildung und Forschung, Grant/Award Number: 03G0270A

Abstract

The export of neritic material from the top of carbonate platforms is a key process in the construction of their slopes. However, our knowledge of the supply pattern of materials from platforms is dominantly based on platforms lying in the euphotic zone during the present sea-level highstand. This is a somewhat biased perspective as through geological time not all platforms were euphotic. The Saya de Malha Bank in the Mascarene Plateau is an example of a modern mesophotic carbonate platform, and as such, its flooding and export patterns differ from those of euphotic ones. Using cores collected on the western slope of the Saya de Malha Bank, the export patterns of the platform since the last glacial maximum were explored. Material on the platform edge is winnowed and transported to the slope by multiple possible processes. The material on the platform is a combination of high and low magnesium calcite as well as high and low strontium aragonite, integrating pelagic and neritic sources. The ratio of these constituents varies over time with changes in the platform production capability as it was flooded and drowned during the Holocene transgression. The material from the platform is transported in both confined flows, mainly during lowstands, and unconfined flows, mainly during late transgression and early highstand. In the present state of the highstand, supply may have diminished, leading to erosion of the canyon shoulders.

KEYWORDS

aragonite, high Mg calcite, highstand shedding, Holocene, Pleistocene, SO270

This is an open access article under the terms of the [Creative Commons Attribution](https://creativecommons.org/licenses/by/4.0/) License, which permits use, distribution and reproduction in any medium, provided the original work is properly cited.

© 2024 The Authors. *The Depositional Record* published by John Wiley & Sons Ltd on behalf of International Association of Sedimentologists.

1 | INTRODUCTION

The deposits accumulated on the flanks of tropical carbonate platforms (T-factory sensu Schlager, 2003) are important palaeoclimate and palaeoceanographic recorders. These periplatform deposits consist of pelagic material from the water column and neritic material from the shallow-water areas on top of the platform. The supply of neritic carbonate has a unique fingerprint, as it is rich in high strontium aragonite (HSA) and high magnesium calcite (HMC), and carries a unique carbon isotope signal (Bialik, Reolid, et al., 2020; Schlager et al., 1994; Swart et al., 2019). These features in turn can be reflected in the observed patterns in the rock record as variations in exported HSA and HMC may impact the lithified product through differential diagenesis (Nohl et al., 2018, 2021). The supply of this neritic material is considered to occur predominantly during periods of sea-level highstand, when the platform top is flooded. Resulting deposits bear sea-level controlled variations in aragonite abundance described as 'aragonite cycles' (Droxler et al., 1983; Reijmer et al., 1988; Rendle et al., 2000; Reuning et al., 2006). These mineralogical variations can be identified in recent calcareous sediments such as those of the Bahamas and Belize (Boardman et al., 1986; Gischler & Zingeler, 2002) and the Great Barrier Reef (GBR; Dunbar & Dickens, 2003). Some aragonite and HMC are lost to dissolution early in the diagenetic process (Dix & Mullins, 1988a, 1988b; Sulpis et al., 2021, 2022; Swart & Guzikowski, 1988), but in the most recent deposits, the different carbonate minerals remain mostly preserved. Dissolution, however, increases porewater alkalinity and preserves the bulk carbonate mineralogy of the sediment, even beneath their lysocline (Sulpis et al., 2022). In deeper burial and geological timescales, the residual aragonite and HMC recrystallise into the more thermodynamically stable low magnesium calcite (LMC; Budd & Hiatt, 1993; Fantle & DePaolo, 2007; Melim et al., 2002). This transformation is apparent in most deep cores of carbonate platforms (Betzler et al., 2017; Eberli et al., 1997; Shipboard Scientific Party, 1997), but is not apparent near the surface. The aragonite on the slope may be neritic HSA or pelagic low strontium aragonite (LSA; Boardman et al., 1986), but the effect on the recrystallisation of aragonite type has not been noted (Dix & Mullins, 1988a, 1988b; Mullins et al., 1985).

Export of HSA and HMC has been demonstrated in many modern active carbonate platforms with a wide active euphotic production area (Alonso-Garcia et al., 2024; Betzler et al., 2016; Counts et al., 2019; Dunbar & Dickens, 2003; Eberli et al., 1997; Lantzsich et al., 2007; Rendle et al., 2000; Slowey et al., 2002). But less is known about this response on the margins of drowned platforms,

that is, carbonate platforms with a top located predominantly below the euphotic depth. These platforms, currently dominantly mesophotic (*ca* 30–150 m water depth, where light is still available but less than *ca* 1% of the levels in euphotic depths) to aphotic (*>ca* 150 m water depth, effectively devoid of light), would theoretically see their euphotic production area increase during a lower sea level state, with parts possibly remaining submerged even in peak lowstand. With higher total production, the potential for export would then increase during lowstand. Shallow flat-topped platforms such as the Bahamas, on the other hand, saw most of their euphotic production area emergent above sea level during glacial times. The impact of these emersions was significant in the short term; it is estimated that around 80% of reef areas were lost due to exposure during the glacial maximum (Kleypas, 1997)—further decreasing the export potential even during the transgression. Given that mesophotic carbonate production is a potentially under accounted major carbonate production area (Amado-Filho et al., 2012), understanding the fate of the inorganic carbon produced by them has major implications for our understanding of the ocean's alkalinity budget.

This work aims to test neritic production export through sea-level lowstand and highstand periods from drowned platforms and the modes of off-platform transport. The target area selected is the drowned Saya de Malha platform in the western Indian Ocean. The Saya de Malha Bank (SMB) was investigated by expedition SO270 of the German research vessel *RV SONNE* in 2019 (Lindhorst et al., 2019), which collected sediment cores on the western (lee side) slope of the platform. Previous studies concentrated on the factors influencing the overall carbonate production (Betzler et al., 2021) and the large-scale drowning process (Betzler et al., 2023). The aim here is to build on top of that existing knowledge and explore the export patterns from the SMB as a model for mesophotic carbonate platforms.

2 | GEOLOGICAL SETTING

Located in the Western Indian Ocean between the Seychelles (4°S) and Mauritius (20°S), the Mascarene Plateau (Figure 1A) is the world's second largest isolated carbonate platform (about 104,aa510 km²), with the Great Bahamas Bank being the first. It formed since the Eocene on top of the aseismic Mascarene Ridge, which is genetically linked to the Réunion hotspot (Duncan & Hargraves, 1990; Meyerhoff & Kamen-Kaye, 1981). Geodynamically, the plateau basement represents a faulted composite arc comprising micro-continent blocks and volcanic structures (Fisher et al., 1967). The SMB

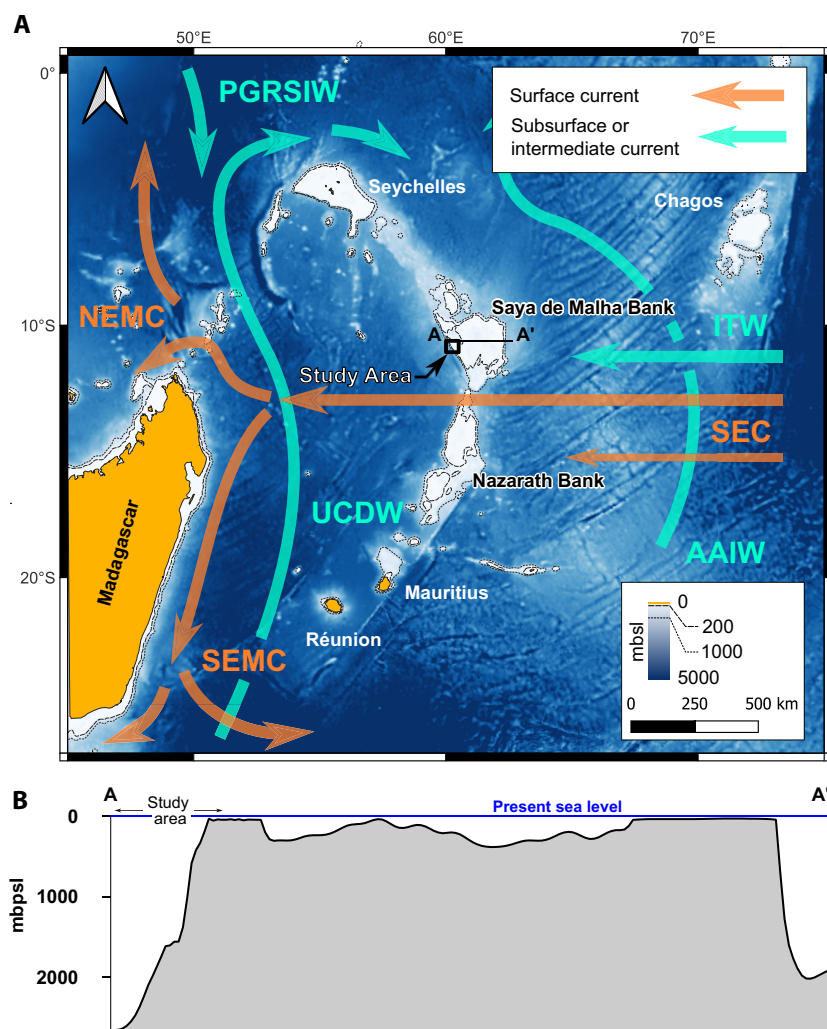


FIGURE 1 Location, structure and oceanography of the SMB. (A) ETOPO Global Relief Model (Amante & Eakins, 2009) bathymetric map of the Mascarene Plateau and surrounding region with main oceanographic elements (Betzler et al., 2021; New et al., 2005). (B) Section across the Saya de Malha Bank (see (A) for location) with position of core GC59. AAIW, Antarctic intermediate water; ITW, Indonesian throughflow; NEMC, north-east Madagascar current; SEC, south equatorial current; SEMC, south-east Madagascar current; UCDW, upper circumpolar deep water.

is the largest of the nine carbonate banks that form the Mascarene Plateau. First described by the Percy Sladen Trust Expedition in 1905 (Rathbun, 1911), the sea floor of the SMB was sampled and mapped in detail by Soviet fishery surveys in the 1960s (Travin, 1968) and 1980s (Fedorov et al., 1980). The bank hosts a shallow submerged ring reef (8 m deep in the shallowest part, and located at an average water depth of 40 m) open to the south, a shallow lagoon (40–100 m), a deep lagoon (100–200 m) and an attached limestone plateau to the south in deeper waters (Betzler et al., 2021, 2023; Fedorov et al., 1980; Vortsepneva, 2008). While mapping is still limited, based on available data the mean depth of the platform top is around 120 m below present sea level. Following the drowning of a larger ancient platform, the modern top of SMB is located in the mesophotic depth-range and below (Betzler et al., 2021, 2023). The resulting bathymetry, from east (windward) to west (leeward) is a steep margin, followed by a narrow plateau and declining reef terraces; a basin in the centre of the bank; continuing west shallower parts are followed by an extended gentler slope (Figure 1B).

The Mascarene Plateau is bathed by the South Equatorial Current (SEC, Figure 1A) that splits and bends around the platforms (New et al., 2005). At the surface, the SEC passes across the SMB from east to west. The surface waters are nutrient-poor, tropical surface waters, which transition to less oxygenated and more nutrient-rich water across the mesophotic zone (Betzler et al., 2021; Lindhorst et al., 2019).

3 | METHODS

3.1 | Data collection and sampling

All data and samples were collected as part of expedition SO270 aboard RV SONNE in September–October 2019 (Lindhorst et al., 2019). Bathymetric data were acquired using the hull-mounted Kongsberg EM122 multibeam systems of RV SONNE at a cruising speed of 5.5–8 km over ground. Equidistant beam spacing and dual swath mode were used for all lines, and transmit fans were stabilised for roll, pitch and yaw. Sound-velocity profiles and

salinity profiles of the water column were obtained from conductivity–temperature–depth probe measurements and by using XSV-02 probes (Lockheed Martin, Sippican Inc.). The software Qimera (QPS software) was used for onboard processing of multibeam data. All bathymetric data were corrected for astronomical tides.

Sub-bottom profiles were recorded using the ship hull-mounted parametric sediment echosounder, Atlas Parasound PS70 (Teledyne RESON GmbH). The system makes use of the parametric effect caused by the interference of the two frequencies in the water column (Westervelt, 1963). The desired primary high frequency was 18 kHz, the secondary low frequency was 4 kHz. The PS70 was operated in single pulse mode with a transducer voltage of 100–120 V. For processing, data were converted to SEG-Y format using the tool ps32segy (Hanno Keil, University of Bremen, Germany). Data processing was done using the software ReflexW (Sandmeier Software) and comprises data editing, compensation for trace header delay, gain adjustment (using automatic gain control) and along-profile amplitude normalisation. Time–depth conversion of Parasound data was done with a standard sound velocity of 1500 ms^{-1} for unconsolidated sediments.

Sediment core localities were selected based on sea floor mapping and sub-sea floor (Lindhorst et al., 2019). Box cores were collected across the entire platform (Figure 2). Three gravity cores were also taken: gravity core SO270_059-5GC ($60.0414^\circ\text{E}/10.9257^\circ\text{S}$, recovery 5.46 m) was recovered from a water depth of 2506 mbsl on the western slope of the SMB (Figures 1B and 3A); cores SO270_063-3GC ($60.1662^\circ\text{E}/10.8329^\circ\text{S}$, 697 mbsl, recovery 4.6 m) and SO270_064-5GC ($60.1703^\circ\text{E}/10.8491^\circ\text{S}$, 1275 mbsl, recovery 4.3 m) were collected from further upslope (Figure 3A). The surface sediments were also retrieved at gravity core localities using a box corer (Lindhorst et al., 2019; Betzler et al., 2023). All cores consist of un lithified sediment and were split and described on-board. Textural classification follows the Dunham (1962) nomenclature. Downcore sediment colour and reflectivity (L^*) were measured each centimetre using a handheld Konica Minolta CM-700d colour scanner. Colour scan data were calibrated and processed using the software SpectraMagic NX pro. Cores were sampled each 1 cm for grain size analysis and each 10 cm for carbonate mineralogy and stable isotope analysis. Depth downcore is reported as metres below sea floor (msbf) or centimetres below sea floor (cmbsf).

3.2 | Sediment sample analysis

X-ray diffraction (XRD) analysis was carried out at the University of Haifa (Israel) using a Rigaku MiniFlex 600 benchtop XRD with a Cu source at 30 kV/10 mA from 3°

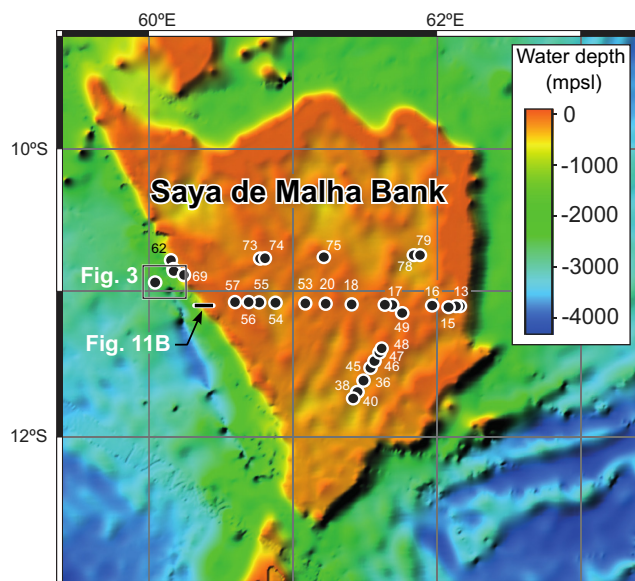


FIGURE 2 Bathymetric map of the SMB platform (GEBCO) showing the location of box cores analysed for surface mineralogy (Table 1) and other cores discussed in the text. The frame shows the location of Figure 3. Line indicates the location of the Parasound line shown in Figure 11B.

to 70° , in 0.05° increments by point detector. Due to the very high carbonate content, only the relative ratio of the carbonate fractions (Aragonite, HMC, LMC) was determined. Analysis was carried out on surface samples from boxcores as well as every 5 cm along core SO270_059-5GC. Fractions were calculated following the relative intensity ratio method (Hubbard & Snyder, 1988) with Rigaku PDXL software with values taken from the PDF2 database (International Centre for Diffraction Data).

Grain-size distributions were determined at the University of Hamburg (Germany) using a laser-diffraction particle-sizer (Sympatec HELOS/KF Magic; range $0.5\text{--}3200 \mu\text{m}$, 32 grain-size classes, particle sizes $0.5\text{--}18 \mu\text{m}$ accumulated in the first class). Prior to measurement, bulk samples (1.5 cm^3 each) were suspended in water using tetra-sodium diphosphate decahydrate as a dispersing agent. To ensure accuracy of measurements, an in-house grain-size standard was measured daily (standard deviation $<3.3 \mu\text{m}$). Grain-size statistics are based on the graphical method (Folk & Ward, 1957), calculated using Gradistat (Blott & Pye, 2001).

Cores SO270_059-5GC (2506 mbsl) and SO270_063-3GC (697 mbsl) were sampled every 10 cm; samples were freeze dried and wet-sieved. For stable isotope analyses, 12 specimens of the planktonic foraminifer *Globigerinoides ruber* were selected from the size fraction $>250 \mu\text{m}$. Stable isotope measurements were done with a Finnigan MAT 253 mass spectrometer coupled with a Carbo-Kiel IV device for CO_2 preparation

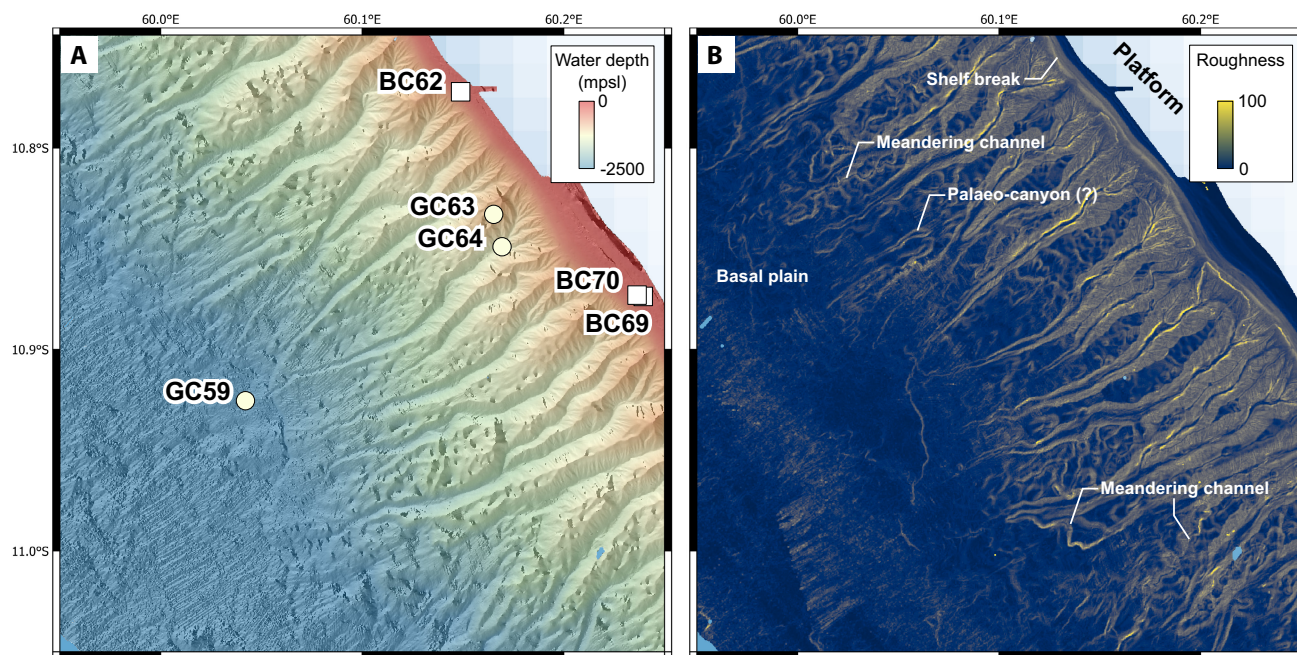


FIGURE 3 Detailed multibeam bathymetry of the mapped portion on the western slope of the SMB. (A) Shaded relief bathymetric map showing the locations of cores GC59, GC63 and GC64 as well as box cores BC62, BC69 and BC70. (B) Roughness attribute of the map shown in (A) with indicators for specific bathymetric features. Roughness is the degree of irregularity of the surface and is calculated by the largest inter-cell difference of a central pixel and its surrounding cell.

from carbonate samples at the Leibniz Laboratory for Radiometric Dating and Stable Isotope Research at the Christian-Albrechts-University (Kiel, Germany). Accuracy of stable isotope measurements is reported by the laboratory to be better than $\pm 0.08\%$ for oxygen isotopes and better than $\pm 0.05\%$ for carbon isotopes. Data on grain size, stable isotopes and carbonate mineralogy is included as supplement 1 (available online as part of: [10.6084/m9.figshare.20000396](https://doi.org/10.6084/m9.figshare.20000396)).

3.3 | X-ray fluorescence core scanning

Cores SO270-59-5GC, SO270_063-3GC and SO270_064-5GC were XRF scanned at the X-ray fluorescence (XRF) Core Scanner laboratory at MARUM (Bremen, Germany) using an AVAATECH series 2 core scanner with an Oxford Instruments XTF5011 X-Ray Tube 93057 and a Canberra X-PIPS Silicon Drift Detector (SDD; Model SXD 15C-150-500). Scans were carried out at 1 cm resolution at 30 kV/1.0 mA and 10 kV/0.15 mA, both with 10 s integration time. Following data quality check of processed data Br, Sr, Ca, Fe and Si were determined to be reliable. The Sr/Ca ratio is considered here as a proxy for the flux of neritic sources HSA (Bialik, Reolid, et al., 2020; Boardman et al., 1986; Counts et al., 2019; Milliman et al., 1993); the Si/Fe ratio as a proxy for the flux of biogenic silica (Bialik,

Reolid, et al., 2020), consisting of diatoms, radiolarian and sponge spicules—the former two being a product of higher nutrient states, with implicit planktonic productivity; the Br/Ca ratio serves as a proxy for the primary productivity and the organic flux (Caley et al., 2011; Ren et al., 2009); and the Fe/Ca ratio is seen as a proxy for terrestrial flux. All XRF data are included as Supplement 2 (available online as part of: [10.6084/m9.figshare.20000396.v1](https://doi.org/10.6084/m9.figshare.20000396.v1)).

3.4 | ^{14}C ages and age estimation

Absolute sediment ages were constrained using calibrated ^{14}C ages (see Supplement 3: [10.6084/m9.figshare.20000396.v1](https://doi.org/10.6084/m9.figshare.20000396.v1)) measured on foraminifer tests. Measurements were done by Beta Analytics (Florida, USA) and calibration was carried out using OxCal (v 4.4; University of Oxford) and the Marine20 calibration curve (Heaton et al., 2020). Marine reservoir corrections in the south-eastern Indian Ocean strongly vary with water masses. Local reservoir ages (ΔR) from pre-bomb bivalve shells collected on the Seychelles and Mauritius, for example, vary between ca -80 and 300 years (Southon et al., 2002). Samples used in this study originate from different water depths and their local reservoir age is unknown. Due to this uncertainty, the local reservoir age (dR) is considered to be 0. Three radiocarbon ages were obtained from core SO270_059-5GC

(abbr. GC59) and two each from SO270_063-3GC (abbr. GC63) and SO270_064-5GC (abbr. GC64). In the absence of any comparable data from the region, extrapolation of these ages, assuming a modern core top, was carried out by correlating the oxygen isotope data against the LR04 global stack (Lisiecki & Raymo, 2005; see Supplementary material). Allowing for offset, the curves exhibit a good fit for the last 34 kyr ($r=0.95$, $p<0.01$, $n=34$). A limited age model was also generated for GC63. However, an age reversal in GC64 (possibly due to reworking) did not allow a robust age model to be established for that core. Given these limitations, this study focussed on time period rather than the exact age, as discussed later.

4 | RESULTS AND INTERPRETATION

4.1 | Seafloor morphology and sedimentology

Towards the western margin, the SMB retains a low angle, near flat surface until a water depth of 215–250

mbsl (Figures 1B, 2 and 3A). The edge of the platform is relatively flat with some platform-edge parallel features. The sediment size on the platform edge ranged between medium to coarse sand (BC62, 99 mbsl, Figure 4A,B), coarse sand (BC70, 87 mbsl, Figure 4C,D) and very coarse sand to gravel (BC69, 81 mbsl, Figure 4E,F). The sediment consists of planktonic foraminifera, small and larger benthic foraminifera (LBF), coralline algae (notably in BC69 as small rhodoliths), pteropods, octocoral sclerites, echinoid and bryozoan fragments, as well as sponge and ascidian spicules in the fine fraction. Traces of *Halimeda* were found in BC62 and traces of scleractinian corals were found in BC69 and BD70.

The surface mineralogy of the platform is dominated by carbonates comprised of varying amounts of aragonite, LMC and HMC (Table 1). Aragonite does not exhibit any clear water depth dependence across the platform (Figure 5A). Both the highest and lowest abundance of aragonite is encountered in shallower water depths. The high shallow-water aragonite is found in the eastern side of the platform as the low shallow-depth aragonite occurs in the western part of the platform. At greater water depth (>150 m), no clear effect of water depth can be discerned.

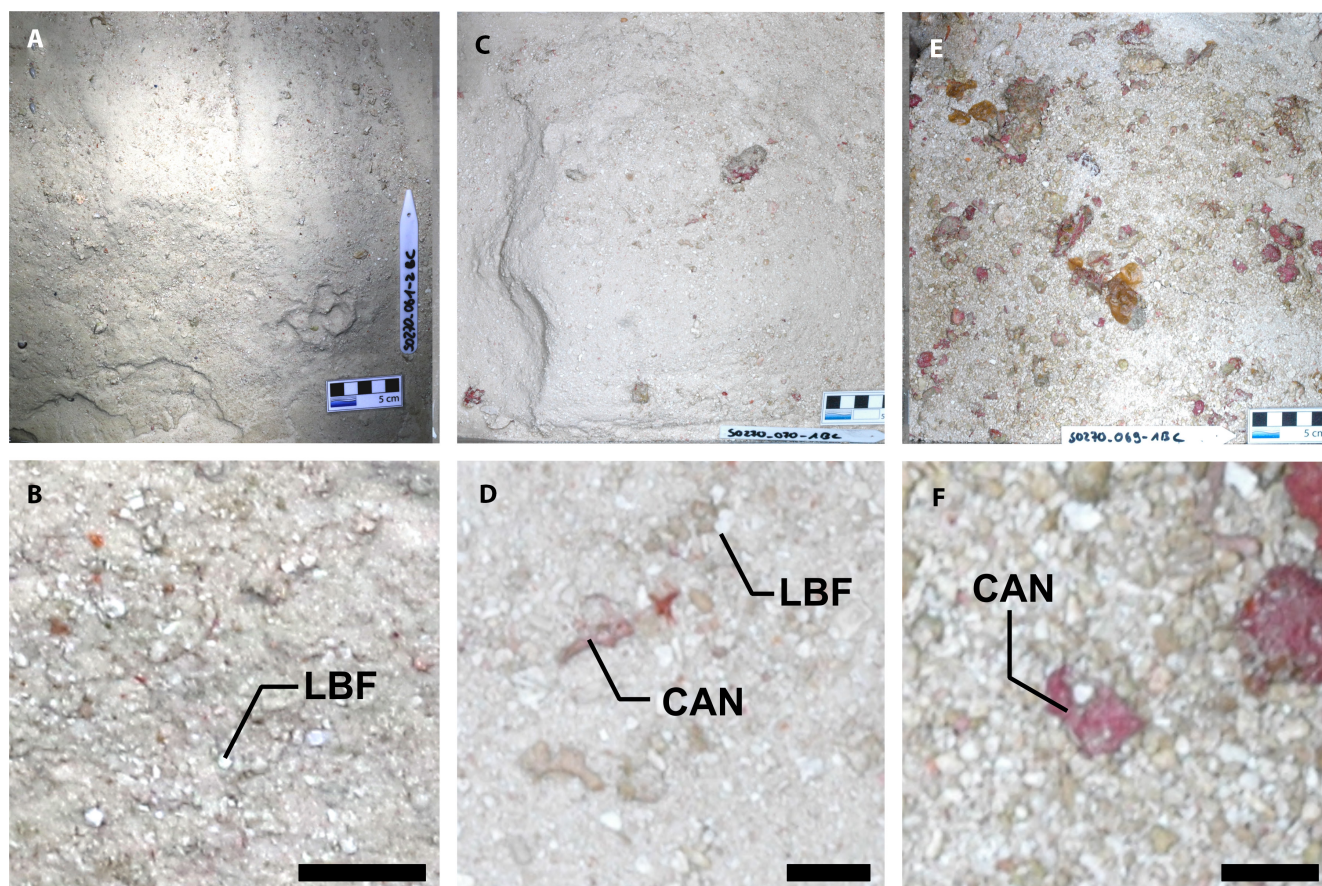


FIGURE 4 Photographs of the box core surface (overview and close-up) for BC62 (A, B), BC70 (C, D) and BC69 (E, F). Scale card in (A), (C) and (E) is 5 cm. Scale bar shown in (B), (D) and (F) is 1 cm. CAN, coralline algae nodule, LBF, larger benthic foraminifera.

TABLE 1 Location, water depth and mineralogical fraction of the carbonate phase in surface samples across the SMB platform.

Station	Long (°E)	Lat (°N)	Water depth (mbsl)	%Aragonite	%HMC	%LMC	%Calcite (total)
BC12	62.244	-11.095	262.5	43.7	34.6	21.7	56.3
BC13	62.132	-11.093	141.0	48.3	34.1	17.8	51.9
BC14	62.103	-11.092	96.5	52.3	30.3	17.3	47.6
BC15	61.940	-11.089	46.8	25.3	52.0	22.6	74.6
BC16	62.051	-11.099	60.2	28.9	55.2	15.7	70.9
BC17	61.665	-11.084	95.0	35.3	36.4	28.1	64.5
BC18	61.615	-11.082	102.7	46.3	36.0	18.7	54.7
BC19	61.389	-11.078	117.6	34.9	38.2	26.8	65.0
BC20	61.211	-11.074	78.9	28.0	40.1	31.7	71.8
BC36	61.469	-11.612	209.7	37.5	36.7	25.7	62.4
BC38	61.426	-11.694	243.2	38.8	15.0	46.0	61.0
BC40	61.398	-11.737	256.5	31.2	33.2	36.1	69.3
BC45	61.518	-11.523	172.3	31.5	45.8	22.5	68.3
BC46	61.545	-11.475	143.8	38.4	38.7	22.8	61.5
BC47	61.579	-11.415	125.5	42.9	32.6	24.3	56.9
BC48	61.594	-11.388	117.4	45.2	35.4	19.3	54.7
BC49	61.734	-11.140	96.7	41.2	35.7	23.0	58.7
BC53	61.072	-11.072	125.4	32.4	24.6	42.9	67.5
BC54	60.867	-11.068	139.0	25.1	35.2	39.5	74.7
BC55	60.755	-11.066	61.3	23.2	42.4	34.2	76.6
BC56	60.683	-11.064	74.4	31.2	37.1	31.6	68.7
BC57	60.589	-11.062	34.6	27.1	53.4	19.4	72.8
BC62	60.150	-10.771	99.1	26.7	38.6	34.6	73.2
BC74	60.794	-10.758	117.7	27.4	42.4	30.1	72.5
BC75	61.196	-10.750	126.2	35.3	23.5	41.0	64.5
BC78	61.814	-10.737	37.2	46.3	39.6	14.0	53.6
BC79	61.857	-10.737	65.0	47.2	36.9	16.3	53.2
GC59	60.042	-10.926	2506.0	29.0	20.9	50.0	70.9

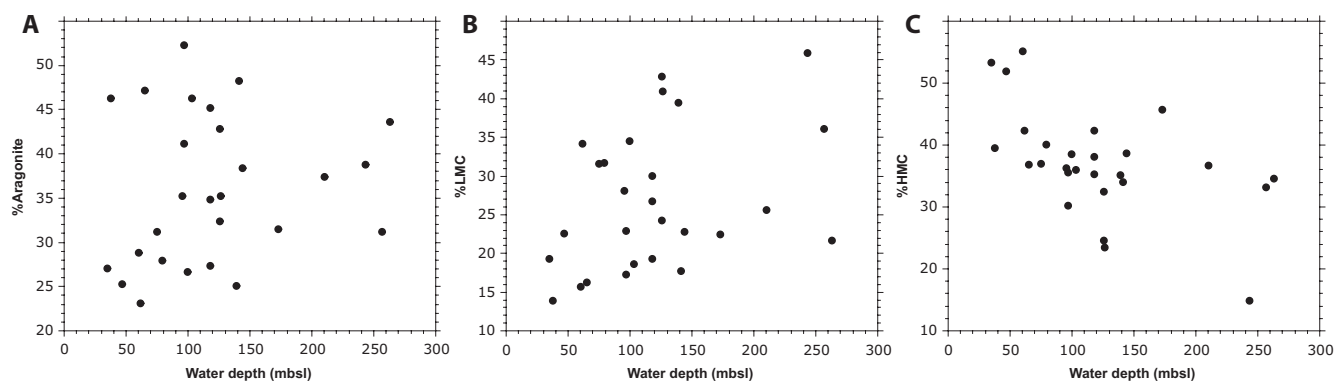


FIGURE 5 Trends in surface mineralogy along depth of the SMB platform for (A) aragonite, (B) LMC and (C) HMC.

The LMC abundance (Figure 5B) and HMC abundance (Figure 5C) appear more related to water depth. The LMC abundance generally increases with water depth,

and HMC decreases. However, while these trends can visually be discerned, they are not statistically significant. Geographically, trends are slightly more significant, with

aragonite correlating more to latitude ($r=0.79$, $p<0.05$, $n=27$) and HMC more to longitude ($r=0.86$, $p<0.05$, $n=27$). The northern and eastern regions are also the shallower parts of the SMB platform, suggesting that production may indeed be water depth-dependent but modulated by local distribution patterns.

At depth, the plateau transitions over a wide and well-defined margin into a canyon-excavated slope, separated by ridges. The ridges vary in width, from more than 1 km to several tens of metres. The canyon heads are formed by a narrow and localised catchment; the horizontal span of the canyons averages 2612 ± 844 m ($n=24$). Tributaries are funnelled into the main canyons at depths of around 1400–1600 mbsl. Some canyons are detached from the uppermost platform slope, possibly being abandoned palaeo-canyons (Figure 3B). Canyon floors are positioned up to 500 m lower as their shoulders and channel meandering is locally present at depths exceeding 2000 mbsl but it is not a characteristic feature of the system. Canyon courses are for the most part straight and confined, and $15,671 \pm 2422$ m ($n=17$) long on average. For the most part, the track of the canyons is perpendicular to the platforms edge. In some canyons, at a depth of *ca* 1000 m, the canyon channel changes direction and bends. This bending is towards the north, at times developing a meandering nature (Figure 3B). The main channels terminate at water depths of around 2500–2700 mbsl, where they transfer into low-relief sedimentary fans that are often amalgamated and fed by more than one canyon. Core GC59 recovered the sedimentary succession of a lobe in one of these fans.

The platform slope has a mean inclination of 5.7° in the slope segments separating the areas excavated by the canyons (Figure 3B). The elevated, unexcavated portions of the slope exhibit an irregular surface, formed by local drainless depressions with a steep upslope termination and a gentler downslope flank. Steep steps are arcuate in shape. Core GC63 is located in one of these morphological depressions, whereas core GC64 was taken from the adjacent channel floor (Figure 3A).

Cores GC59, GC63 and GC64 capture the main depositional settings on the western slope of the SMB. The sediment of all three cores (Figure 6) is rich in carbonate in the size fraction $<63 \mu\text{m}$ (i.e., fine). The sediment hosts foraminifera (dominantly planktonic) and pteropods in its sandy and coarser grained fractions. In core GC64 (canyon head), sandy layers are present, and the sand fraction ($63 \mu\text{m}$ to 2 mm) is dominant in some intervals. Whereas in core GC63 (canyon shoulder), fine-grained hemipelagic material prevails. Core GC59 (basin lobe) exhibits a mixture of these two modes.

Down to 3.6 mbsf the core GC59 is a packstone with sand-sized bioclasts being more dominant between 1.8 and 2.7 mbsf, with mudstone–wackestone and

wackestone–packstone intervals between 1.4 and 1.8 mbsf and about 2.2–2.4 mbsf, respectively. Between 0.1 and 0.2 mbsf and around 1.0 mbsf grainstone intervals with radiolarians are present. Radiolarians were also found at 2.2 mbsf associated with a coarser-grained interval. While visually, the sediment appears as a grainstone to packstone, between 2.4 and 2.8 mbsf, the fine fraction increases, and fines dominance persists from 2.8 to 3.6 mbsf. From about 3.6 mbsf, the sediment texture becomes dominantly wackestone to wackestone–packstone. At 1 and 2.20 mbsf, some red algal debris is present. Additionally, bivalves, gastropods, LBF, octocoral sclerites, echinoids, sponge and ascidian spicules were found in the upper part sampled by the box core.

Texture wise, sediment recovered by core GC63 (canyon shoulder) is a packstone until about 4 mbsf, and through this interval, the sand fraction decreases. The sand fraction increases again near the base of the core and packing becomes less dense. The sediment is consistently rich in carbonate mud, with the fine fraction never below 30% and being for the most part higher than 50%. The coarser material found near the base of the core consists of partially cemented unidentified allochems and pteropods. Additionally, bivalves, gastropods, octocoral sclerites, echinoids, bryozoans, serpulid fragments and sponge and ascidian spicules were found in the upper part sampled by the box core.

The top 10 cm of core GC64 (canyon head) is a floatstone with a few large pteropods. Further down to a depth of 2 mbsf, the sediment is a wackestone with the fines content increasing downcore. Between 2 and 3 mbsf, the coarser fraction increases, and the sediment texture transfers to a packstone. A grainstone is present between 2.60 and 2.75 mbsf, hosting radiolarians, as well as gastropod, red algal and bryozoan fragments. These coarser grains become dominant in some samples, which are free of fines. Below 3 mbsf, the fine fraction becomes more dominant, and the sediment texture is a wackestone except for two packstone intervals between 3.4 and 3.7 mbsf. Additionally, bivalves, gastropods, LBF, octocoral sclerites, echinoids, sponge spicules, serpulid and *Halimeda* fragments were found in the upper part sampled by the box core.

4.2 | Sedimentary intervals

Core GC59 (see supplement for age model) is divided into five main sedimentary intervals labelled from 1 (youngest) to 5 (oldest). Interval (1) spans the period covering the end of the African Humid period (AHP) to the present (Figures 6, 7 and 8); (2) the AHP itself (*ca* 15.5–6.5 kyr, *ca* 0.69 mbsf); (3) the period between the last glacial

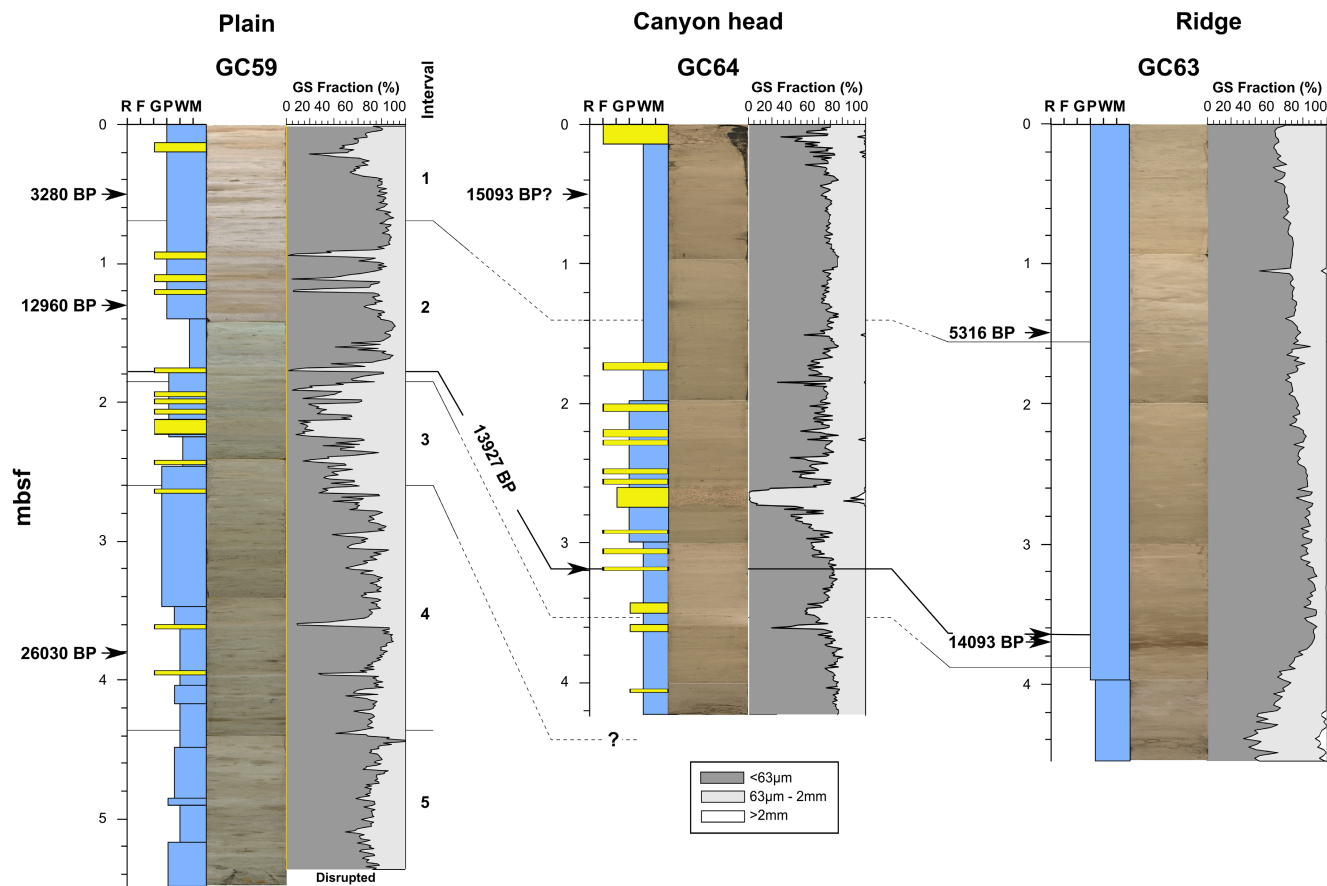


FIGURE 6 Columnar sections of core GC59, GC63 and GC64, showing texture, core photographs and grain size fraction for each core. Radiocarbon ages are noted by arrows with the 13.9 isochron traced between the cores. Legend indicates the grain size (GS) fraction shown next to each core. Note that the texture column on the right refers to visual description of the cut surface of the core and the grain size only to the size fraction in a 1 cm^3 subsample.

maximum (LGM) lowstand and the beginning of the AHP at ca 15.5 kyr (ca 1.87 mbsf); (4) the period of the LGM lowstand (ca 26.5–19.5 kyr BP, ca 2.55 mbsf); and (5) the period from the base of the core (ca 34 kyr BP) to the beginning of the LGM lowstand at ca 26.5 kyr BP (ca 4.35 mbsf). These are delineated here based on sedimentological parameters as well as variations in geochemical properties which allow for correlation between the cores (Figure 6, see text below for details on the characterisation of each interval). With ^{14}C ages used as secondary constraints.

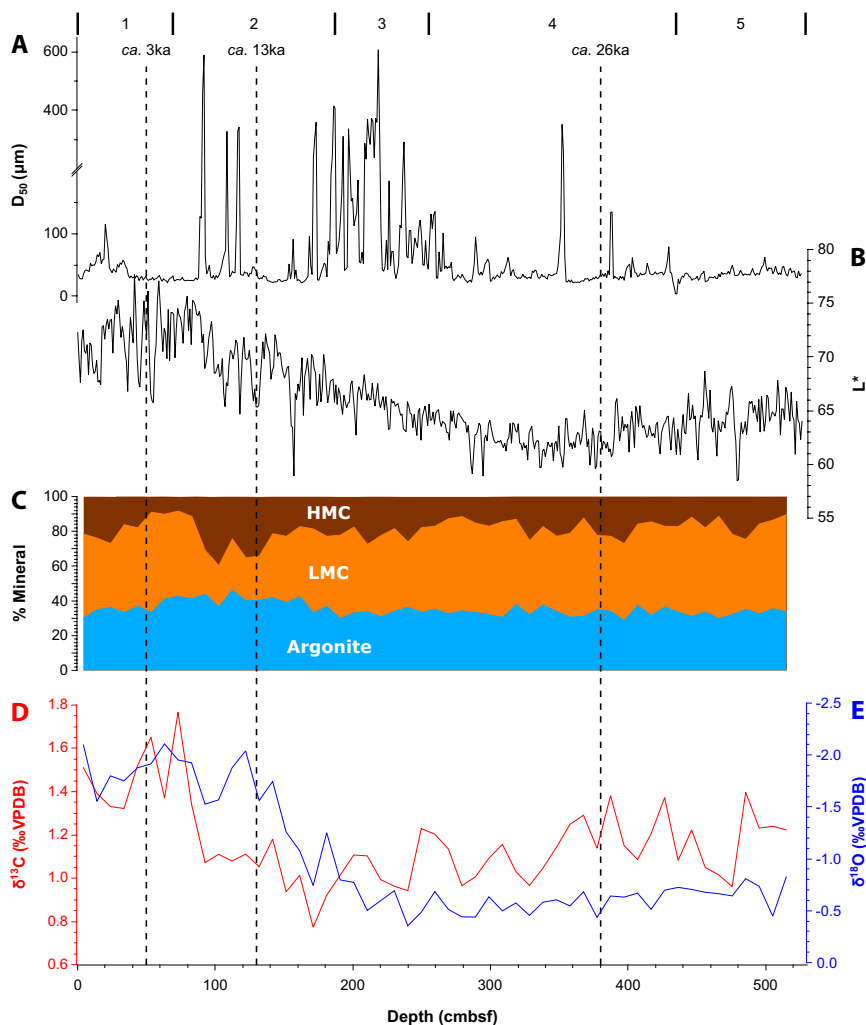
4.3 | Detailed analysis of core SO270_059-5GC

The D_{50} (Figure 7A) coarsens to a maximum in Interval 3, with a few spikes also present in intervals 2 and 4. Lightness value (L^* , Figure 7B) decreases slightly from the base of the core to a minimum in Interval 4 and subsequently increases, reaching a maximum in Interval 1.

The carbonate mineral fraction (Figure 7C) remains stable with LMC being the most abundant form until the beginning of the AHP at which point both HMC and aragonite content increase. The HMC content begins to diminish 7–8 kyr BP and aragonite content decreases in the immediate aftermath of the AHP at which point both HMC and aragonite return to their pre-AHP levels. Oxygen isotope values (Figure 7E) remain relatively stable ($\delta^{18}\text{O} \approx -0.5\text{‰}$) from the base of the core to Interval 3 and subsequently decrease in intervals 3 and 2, stabilising ($\delta^{18}\text{O} \approx -1.7\text{‰}$) around 110 cmbsf and remaining at this level across Interval 1. Planktonic foraminifer (*G. ruber*) carbon isotope values (Figure 7D) remain relatively stable ($\delta^{13}\text{C} \approx 1.0\text{‰}$) until about 8 kyr BP before rising and stabilising on a higher level ($\delta^{13}\text{C} \approx 1.5\text{‰}$). Three ^{14}C ages were obtained in the core, ca 3.3 ± 0.2 ka cal. at 0.5 mbsf, ca 13.0 ± 0.2 ka cal. at 1.3 mbsf and ca 26.0 ± 0.3 ka cal. at 3.8 mbsf.

The Fe/Ca ratio (Figure 8A) remains stable from the base of the core to the base of Interval 3 and then exhibits increased fluctuations through intervals 2 and 1,

FIGURE 7 Depth change in bulk stable isotopes, mineralogy, Lightness value, D₅₀ and ¹⁴C ages along core GC59. Note that the spacing of the ages would suggest a non-linear sedimentation rate.



with an increase near the top of Interval 2. The Br/Ca ratio (Figure 8B) remains stable throughout intervals 4 and 5, then exhibits strong oscillation and decreases to a minimum value in Interval 2, with an increase in Interval 1. The Si/Fe ratio (Figure 8C) oscillates at around a mean value of 4.2 ± 1.0 ($n = 267$) in intervals 4 and 5, then declines to a 2.3 ± 0.8 ($n = 58$) in Interval 3 and increases to 3.6 ± 1.7 ($n = 191$) in intervals 2 and 1, exhibiting stronger and shorter oscillation than before. The Sr/Ca ratio (Figure 8D) increases in two steps, at the base of Interval 3 marked by high values and spikiness and again in Interval 2, rising to a more stable baseline in Interval 1. All elements exhibit a spike between 90 and 97 cmbsf which corresponds to a sand-rich (grainstone) interval.

4.4 | Detailed analysis of core SO270_063-5GC

The D_{50} is at a minimum value of $20 \mu\text{m}$ near the base of Interval 2 (ca 3.75 mbsf) and exhibits a continued increase

since then to a value of $50 \mu\text{m}$ near the top of the core (Figure 9A). Both Fe/Ca and Br/Ca ratios (Figure 9B,C, respectively) exhibit a peak near the base of Interval 2 (ca 3.4–4.0 mbsf) followed by a decline. This peak does not correspond to a minimum in the Ca counts indicating that it does represent an increase in both Br and Fe. The Fe/Ca ratio declines onwards whereas the Br/Ca ratio exhibits a slight increase in Interval 1 (Figure 9C). The Si/Fe ratio (Figure 9D) exhibits an overall flat baseline, punctuated by single intervals with very high values, likely the addition of biogenic silica as no element related to lithogenic input coincides with them. The Sr/Ca ratio increases from Interval 3 to Interval 2 (Figure 9E), reaching a plateau in Interval 2 and diminishes towards the end of this interval with a trend of continued decrease in Interval 1. Through both intervals 1 and 2, punctuated events of increased Sr/Ca ratio are present. They do not appear to represent any input of coarse material as no corresponding change in grain size is observed. Lightness value decreases in the transition from Interval 3 to Interval 2 and then increases to a maximum at the base of Interval 1 (Figure 9F). Planktonic foraminifer (*G. ruber*) carbon isotopes (Figure 9G) exhibit

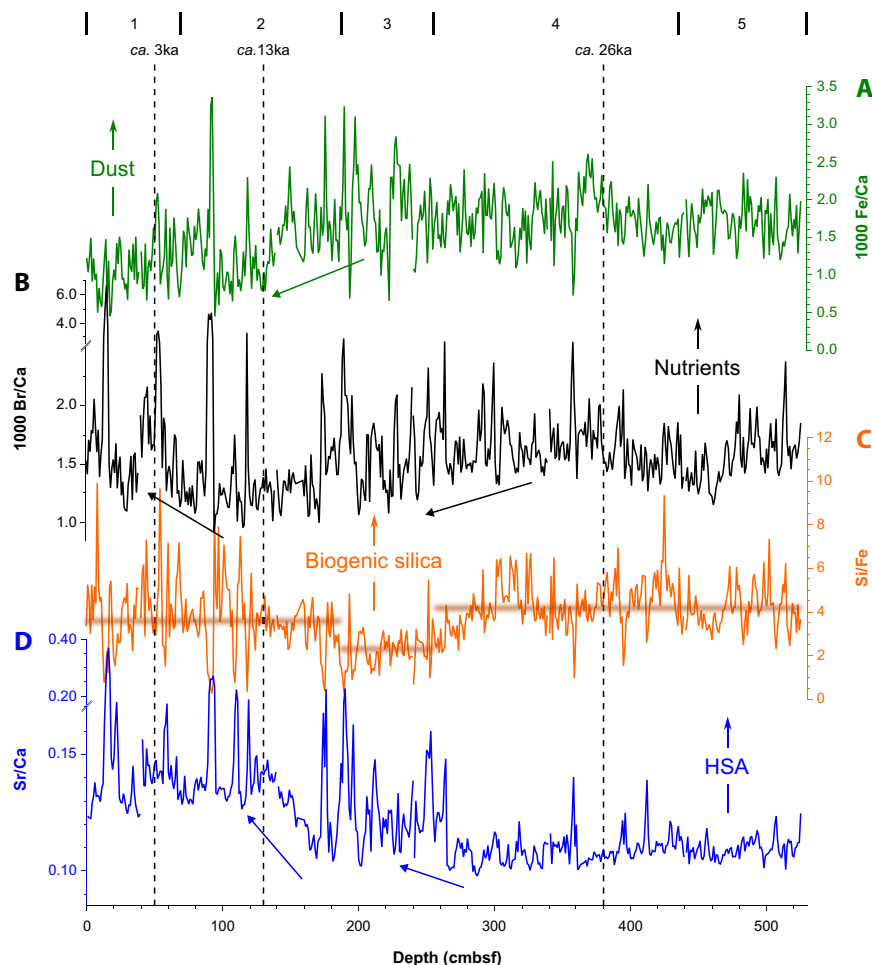


FIGURE 8 Depth change in elemental ratios (Sr/Ca, Si/Fe, Br/Ca and Fe/Ca) and ^{14}C ages along core GC59. Note that the spacing of the ages would suggest a non-linear sedimentation rate.

an increase in value from *ca.* 2.6 mbsf whereas oxygen isotopes (Figure 9H) exhibit an ongoing decline through the entire period. Two ^{14}C values were obtained from core GC63, yielding ages of *ca.* 5.3 ± 0.3 ka cal. at 1.5 mbsf and *ca.* 14.0 ± 0.1 ka cal. at 3.7 mbsf.

4.5 | Detailed analysis of core SO270_064-5GC

The D_{50} across most of the core has a mean value of $45 \pm 10 \mu\text{m}$ ($n = 402$, Figure 10A). This near constant background level is punctuated by four coarse-grained events between *ca.* 0.09 and 0.18 mbsf, *ca.* 1.79 and 1.91 mbsf, *ca.* 2.61 and 2.83 mbsf and *ca.* 3.59 and 3.66 mbsf. These spikes consist of sand-sized and gravel-sized fractions, although the sand fraction makes up around $37 \pm 14\%$ ($n = 421$) of the total grains in the core (Figure 6).

These grain-size patterns are not well reflected in the geochemical data from the XRF scans (Figure 10). Both the Fe/Ca (Figure 10B) and Br/Ca (Figure 10C) records of core GC64 show limited variability. A local minimum in Si/Fe ratios (Figure 10D) is present between *ca.* 2.1 and

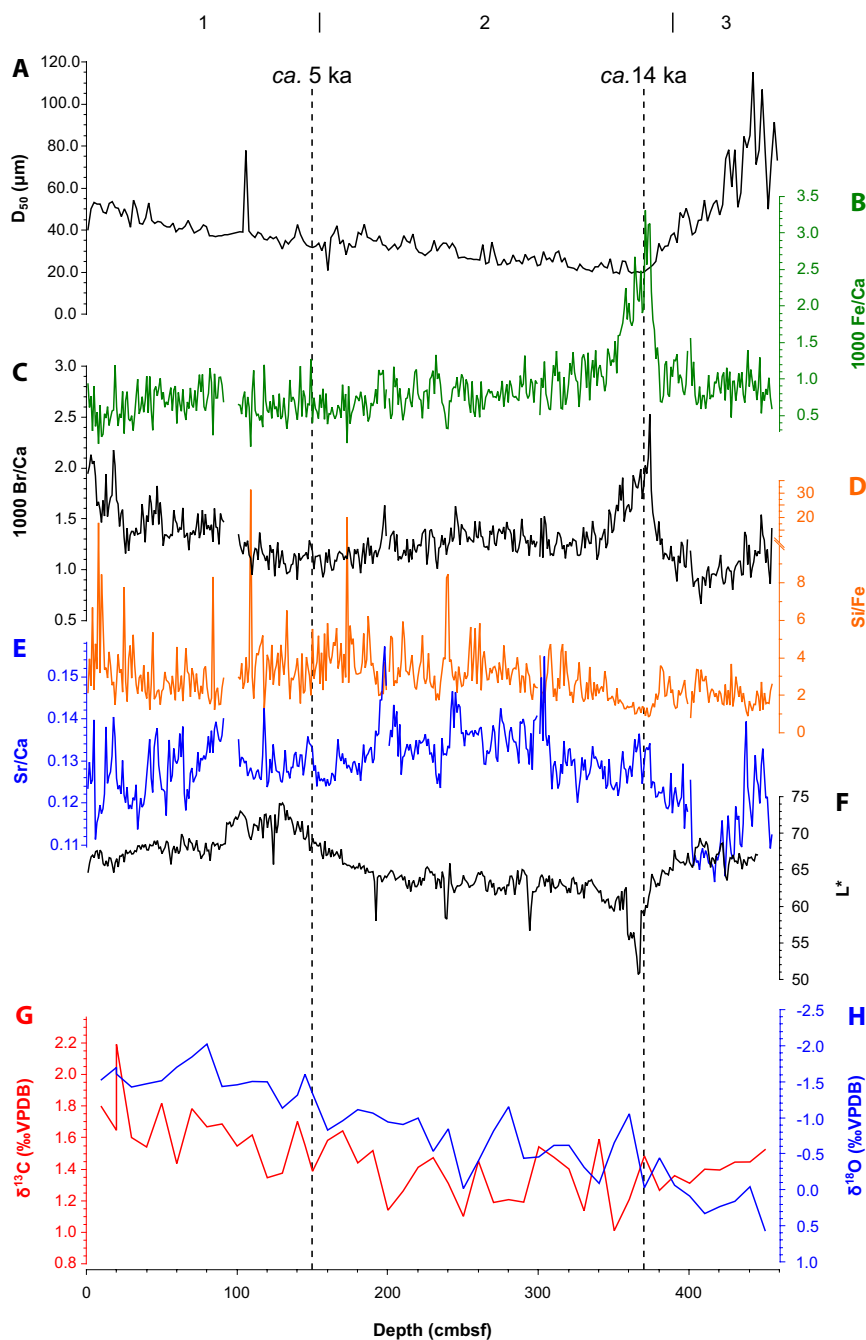
2.7 mbsf, corresponding partially to the largest grain-size spike, but the other spikes lack similar patterns. The Sr/Ca ratios (Figure 10E) exhibit a generally increasing trend across the entire core. This trend does not display any relationship to the grain-size spikes, nor to Lightness value (Figure 10F), showing independent peaks and troughs that do not correlate to any other record generated for this core. Two ^{14}C ages were obtained in core GC64, one at 0.5 mbsf yielding an age of *ca.* 15.1 ± 0.5 ka cal and *ca.* 13.9 ± 0.5 ka cal at 3.2 mbsf.

5 | DISCUSSION

5.1 | Delineation of the highstand and lowstand

Neither the exact age of the top of the cores nor the reservoir ^{14}C time in SMB is known. As such, the exact ages are difficult to determine in the cores and a relative timing must be used. Assuming that the top of the cores is near modern, an argument could be made that Interval 1 represents the post-AHP and Interval 2 the AHP. This would be consistent with the plateau in $\delta^{18}\text{O}$

FIGURE 9 Depth change in D_{50} and elemental ratios (Sr/Ca, Si/Fe, Br/Ca and Fe/Ca), Lightness value and ^{14}C ages along core GC63. Note that the spacing of the ages would suggest a non-linear sedimentation rate.



values for Interval 1 in GC59 and would place Interval 1 as the high sea-level state (highstand), whereas intervals 2 and 3 would represent the phase of sea-level rise. The minimum $\delta^{18}\text{O}$ values in Interval 4 would likely mark it as the LGM, with Interval 5 likely infringing on this period as well. Consequently, these two intervals likely mark the low sea-level state (lowstand). In core GC59, this assumption matches the Sr/Ca trend, which in the Indian Ocean has been shown to correlate with sea level (Alonso-Garcia et al., 2024; Bialik, Reolid, et al., 2020; Counts et al., 2019).

The record in core GC63 is likely younger than 20 kyr BP (see correlation and ages in Figure 6). However, age

control before 14 kyr (*ca.* 3.7 mbsf) is weak. Unlike GC59, where oxygen isotopes could be used to help confirm the age model, in GC63, the interval was too short to fit in a satisfactory way to the global curve. Age reversal in core GC64 (Figure 6) similarly limits the discussion. The 13.9 ka age at 3.2 mbsf appears more reliable but is insufficient to build a robust age model, although it allows an additional shared age datum to be established. Using this correlation and extending the rationale above, these two cores record only the phase of sea-level rise and highstand phases.

Despite these significant uncertainties, on first order, it appears that the sedimentation rate at the top

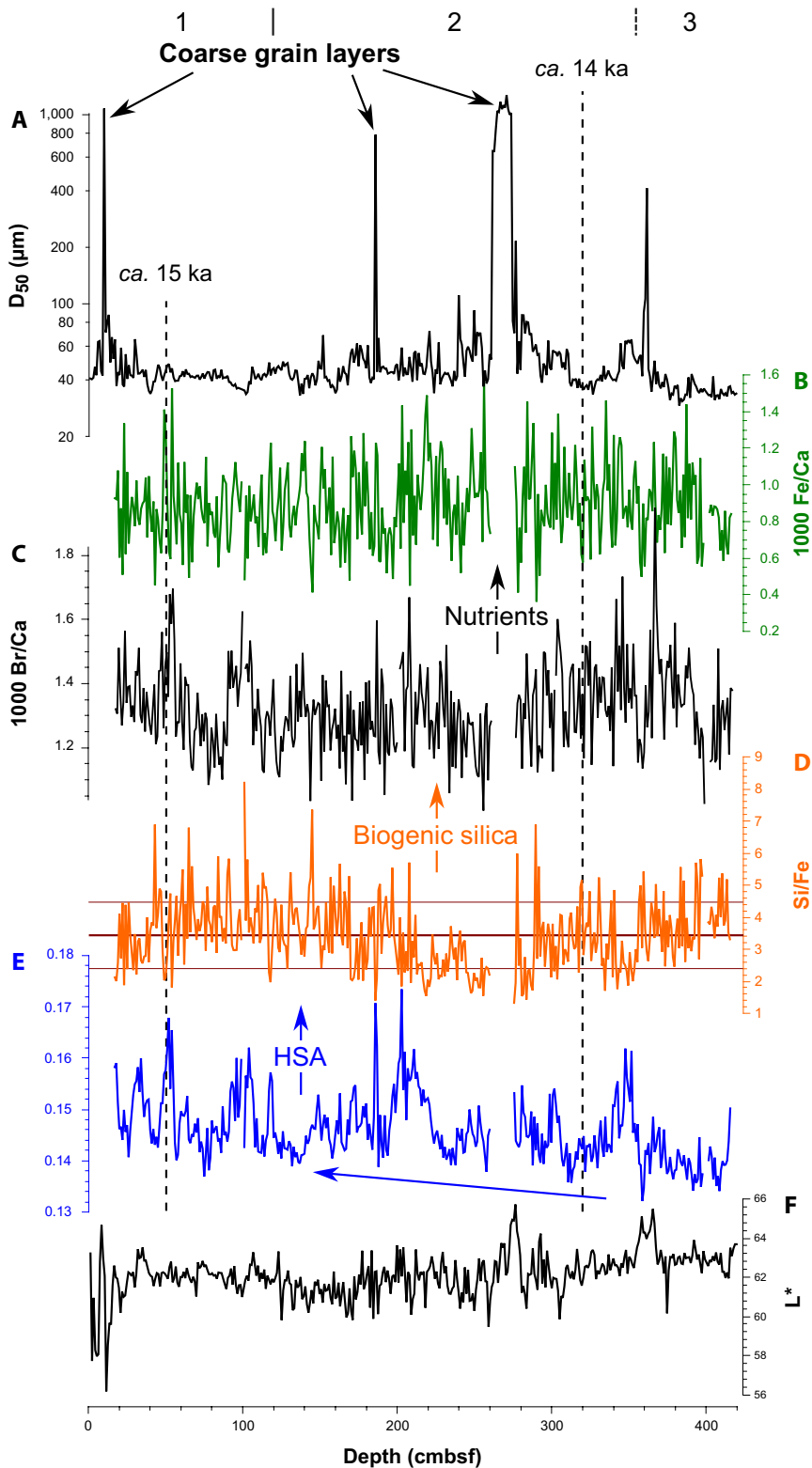


FIGURE 10 Depth change in D_{50} and elemental ratios (Sr/Ca, Si/Fe, Br/Ca and Fe/Ca), Lightness value and ^{14}C ages along core GC64.

of the slope (ridge and canyon head) is nearly twice as high as the canyon discharge on the plain. Using the available age and assuming that the core top is modern, a linear fit rate of *ca.* 0.14 m/kyr would be ascribed to core GC59, *ca.* 0.26 m/kyr to GC63 and *ca.* 0.23 m/kyr to GC64.

5.2 | Modes and configuration of sediment transport

The western slope of the SMB, past the platform edge, consists of two architectural elements: canyons and ridges. The features present on the broader ridges (Figure 3B)

are proposed to reflect downslope creeping submarine landslides. Deposits recovered in Core GC63 are primarily hemipelagic with no indications of mass transport. This absence may be partially attributed to the location being upslope and, thus, a position more likely to be eroded (Pratson et al., 2000). However, the spikes in the Sr/Ca ratio (Figures 8, 9 and 10), likely indicating the introduction of neritic high-strontium aragonite (HSA), suggest the supply of fine-grained material from the platform. The absence of coarse grains in cores GC63 and GC64 suggests that the supply of neritic material takes place in unconfined low-energy flows that cannot transport such coarse material. This fine material is likely winnowed from the platform. In contrast, in core GC59 at the base of the slope, Sr/Ca peaks occur both in coarser and finer grain-size intervals (notably coarse grain size in Interval 3), suggesting also transport by turbidites (possibly localised) as well as fine fraction transport.

The sediment on the platform edge (Figure 4) is rather coarse-grained, without a significant fine fraction, pointing to active, although possibly intermittent, winnowing. The preservation of pigments in coralline algae and foraminifera (Figure 4B,D,F) indicates the material in play is, at least partially, recent. Three possible processes may facilitate this winnowing: deep storm waves, internal waves and bottom currents. It is not likely this material is being winnowed by westbound waters of the SEC, which will be blocked by the eastern edifice of the platform. However, the SEC is deflected northwards in this region (Schott & McCreary, 2001), allowing for northwards-bound bottom currents. The tropical Indian Ocean is prone to tropical cyclones, with over 10 significant cyclones making landfall on the south-eastern African margin per year (Mavume et al., 2010). These cyclones come around the SMB from the east and would push material to the west. However, it is unclear how deep the associated waves could impact the sea floor. During cyclone events in the north-western Indian Ocean, the common wave frequency was measured to be around 0.1 Hz (Sirisha et al., 2015), which would equate to a wavelength of *ca* 156 m—and a wave base of *ca* 78 m. This could be a viable mechanism to transport fine material to depth through hyperpycnal flows (Bialik et al., 2022). But it is not deep enough to scour the sea floor at a depth exceeding 200 m, where the platform margin resides on the western edge. Individual waves may impact at that depth, but the effect of such waves is unclear. Internal waves have been observed on the SMB and their impact documented (Betzler et al., 2023). They are impactful at the depth of the platform edge on the west and can winnow and remobilise sediment. These waves would originate from the south and propagate northwards along the edge of the shelf. Elevated flow velocities have been documented on the western edge of the SMB in comparable depth (Lindhorst et al., 2019), which may be the propagation

of these internal waves or bottom currents. Currently, it is not possible to deconvolve these two elements.

Coarse-grained intervals in both the canyon head (core GC64) and the mouth of the canyon (core GC59) indicate transport in and into the canyon through high-energy focal flows. The presence of neritic components (red algae, LBF, *Halimeda*) indicates that these sites receive material from the platform. The supply of neritic material and occurrence of coarse-grained intervals intercalated with fine-grained ones suggest transport by episodic mass wasting events, driven, perhaps, by major tropical storms. It cannot be excluded that some of this material was eroded from the canyon wall and the platform itself, which may be the source of the older material near the top of core GC64.

The higher sedimentation rate during the sea-level highstand on the canyon flank relative to the canyon head suggests that the less-confined transport mode is common. In this scenario, unconfined flows would lead to more deposition at the head of the slope rather than at its base. However, it is not possible to compare highstand with lowstand sedimentation rates at the head of the slope as no core penetrated to that depth. At the base of the slope (core GC59), the sedimentation rate appears to be higher in the lowstand. Detachment of a canyon from its upslope or downslope elements is usually due to the activity of an adjacent canyon (Figure 3B). The lower sedimentation rate in the channel and the presence of coarse-grained material (Figure 6, core GC63) indicates that transport and winnowing in the conduit continues during the highstand.

5.3 | Changes in accumulation patterns and controls

Examining the various variations in the cores, a temporal pattern of changes in oceanographic conditions and associated supply of material from the platform emerges, driven by changes in the platform area and structure (Figure 11A). During the lowstand (intervals 4 and 5), neritic export was low as evidenced by both the Sr/Ca ratio and the lower amount of both aragonite and HMC. However, the total flux to the toe of the slope was higher. Lower lightness values and higher levels of both Si/Fe and Br/Ca ratios (Figures 7 and 8) point to a higher fraction of pelagic material, possibly promoted by higher dust supply (Figure 8A). The minimum in lightness values during this period (presetting less carbonate and more organic matter/terrestrial material; Poli et al., 2010), similarly support this interpretation. As no change is observed in the elemental or mineralogical data, the shift was likely in the organic input ratio to carbonate. Despite that, short intervals with coarser grain size in Interval 4 (Figure 6) correspond

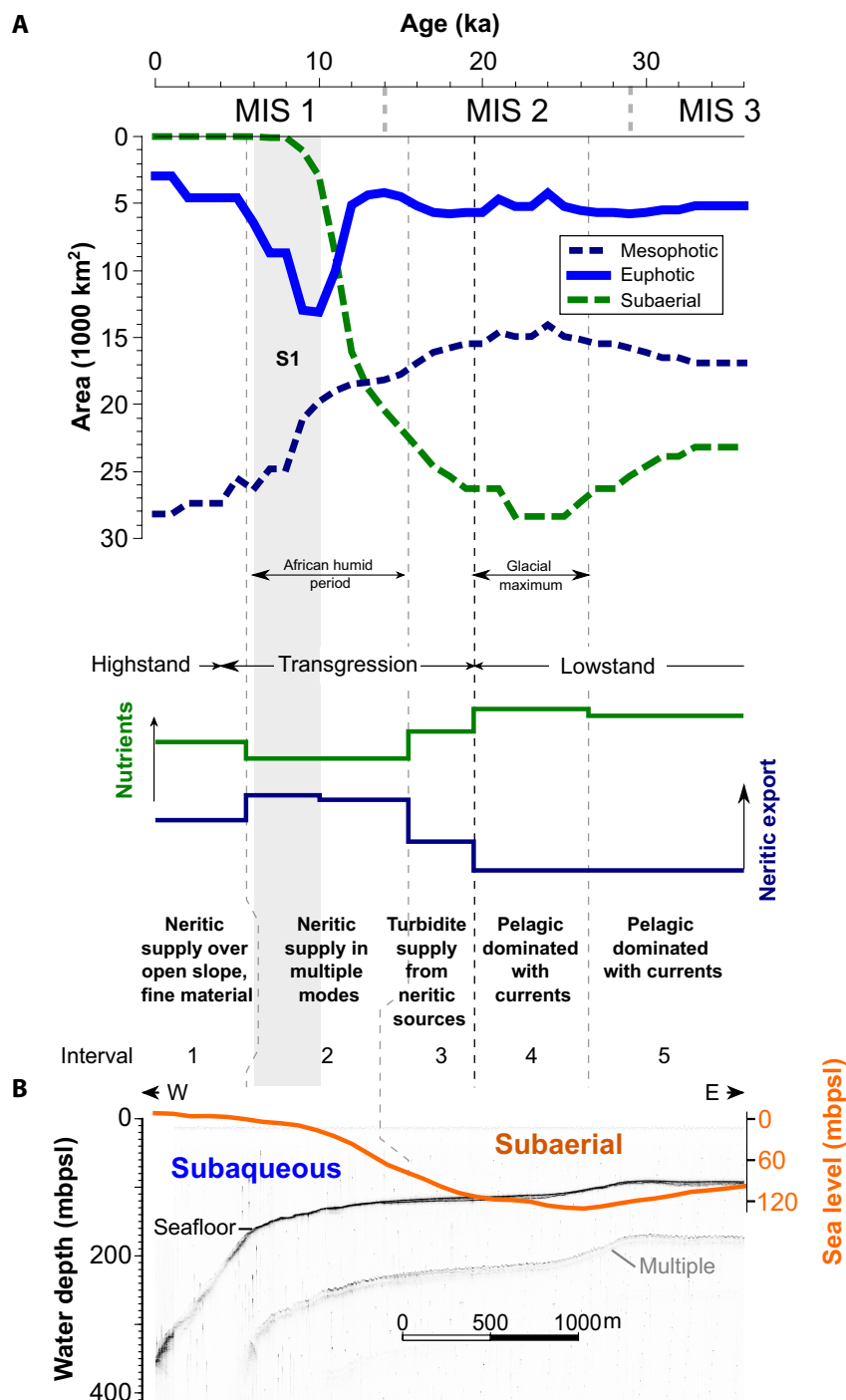


FIGURE 11 (A) Changes in the relative areas of production on the SMB over the period recorded in core GC59 (calculated from GEBCO bathymetric data and sea-level reconstruction by Spratt & Lisiecki, 2015) and corresponding reconstruction of conditions as recorded in the core. (B) Parasound line SO270_PS001 across the western flank of the SMB (Lindhorst et al., 2019) showing the form of the seafloor at the platform edge in the study area, overlain by the sea-level curve (Spratt & Lisiecki, 2016; X-axis as in A). A higher resolution version of the parasound line is available in the supplement.

to a slight increase in the Sr/Ca ratio (Figure 8D) and could indicate localised downslope transport events of neritic material (Figure 12A).

In the transition from the lowstand to sea-level rise (Interval 3), the exposed land area on the SMB decreased, leading to an increase in the mesophotic (30–150 m) domain, however without a clear shift in the size of the euphotic domain (Figure 11A). That said, any area would transition from land first to euphotic and only subsequently to mesophotic, with the transition dependent on the ability of production to keep up with sea-level rise.

With this shift, neritic supply increased as biogenic silica supply declined. The supply of neritic material downslope was in pulses and localised, indicated by the strong oscillation in grain size, likely indicating sediment gravity flows. Neritic material was not retained at the head of the slope, evidenced by the low Sr/Ca ratio in core GC63 (Figure 9F) compared to the base of the slope in core GC59 (Figure 8D). The inconsistency in the Fe/Ca ratio between the plain (GC59) and the ridge (GC63) could be due to different dispersal patterns, but alternatively could be related to monsoonal wind intensity and associated dust influx.

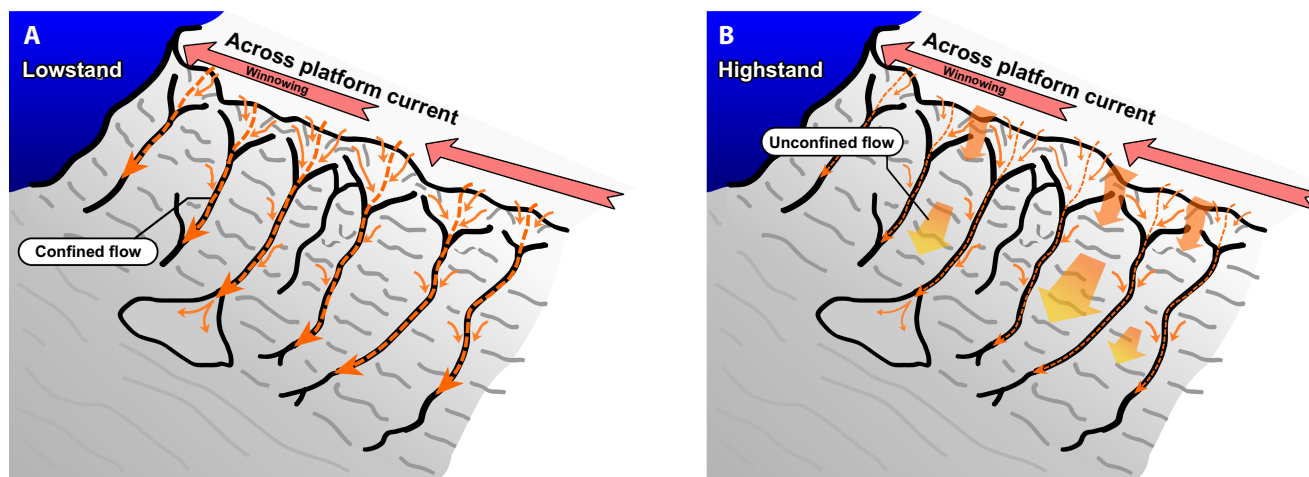


FIGURE 12 Conceptual model for modes of transport along the western slope of the SMB. Dominant channelised transport in (A) lowstand and more spread and unconfined transport during (B) highstand in sea level.

The SMB is an isolated, open-ocean carbonate platform, situated far from potential fluvial input (Figure 1A). With ocean currents from the east, that is, from the open Indian Ocean, and the westward-directed atmospheric circulation of the trade wind belt, terrestrial input is considered to be minor and primarily derived from aeolian dust (Léon & Legrand, 2003). This is in line with the proposed shift in the mode of climate variability with global warming from the lowstand (LGM) towards the highstand (Abram et al., 2020).

That said, the increase in both Br/Ca and Fe/Ca ratios without any depletion in Ca would suggest that productivity is paired with dust. Dust can play an important part in fertilisation of isolated carbonate platforms (Swart et al., 2014). The dust source is unclear as the winds in the low latitude Indian Ocean region over the last 20 kyr come dominantly from the east (Thirumalai et al., 2019), making Australia the mostly likely source, although Middle Eastern dust does reach the region (Kok et al., 2021). Yet both potential sources are thousands of kilometres away. The significant transport distance from likely dust sources suggests the supply was probably highly limited, and as such, the spatial pattern of atmospheric distribution might be stochastic, limited to events rather than a constant supply, and not uniformly spread across the SMB. Some uncertainties do persist, given the unknown provenance of the material on the platform, which may introduce phase lags (Emmermann, 2000; Emmermann et al., 1999; Sepulcre et al., 2017). This is partially also informed by the $\delta^{13}\text{C}$ of the planktonic foraminifera, which does not appear to exhibit a comparable temporal trend between the area near the top of the slope and the base of the slope (Figures 7D and 9G), likely representing spatial variability in the carbon system. This variability might be productivity related, but given the low productivity in the

region it is more likely governed by sea surface temperature (Bemis et al., 2000). This variability within the same latitude could be driven by limited local upwelling or interactions of different water masses.

During Interval 2, still within the transgressive phase, the land area on the SMB likely was significantly reduced (Figure 11A), leading to the expansion of mesophotic areas first and then of euphotic production areas as the rate of sea-level change declined (Spratt & Lisiecki, 2016). This would be a significant contrast with euphotic platforms such as the Bahamas, which were only re-flooded in the latest stage of the transgression into euphotic production mode (Lopez-Gamundi et al., 2022, 2024; Roth & Reijmer, 2004, 2005). During this period, HMC export increased significantly as did overall aragonite supply (Figure 7), with Sr/Ca ratios indicating this aragonite to be neritic HSA (Figure 8D). The increase is more significant at the head of the slope (Figure 9E), which exhibits a higher Sr/Ca ratio at this time. This increase in the head of the slope suggests that the supply was not localised to higher density flows in the canyons. As these events continued, as evidenced by coarser grained size events at the base of the slope (Figure 7A), their frequency increased in Interval 3, which is dominated by coarser grain size events. However, by the beginning of Interval 2, their frequency significantly diminished, which suggests a transition to unconfined flows towards the highstand (Figure 12B), as the Sr/Ca ratio peaks on the ridge (Figure 8E) and in the mouth of the canyon (Figure 10E).

Although HMC forms in both the euphotic zone and the mesophotic zone, the organisms producing it (notably soft corals and calcareous red algae) are more common in mesophotic depths (Benayahu et al., 2019; Grossowicz & Benayahu, 2015; Perrin et al., 1995; Yesson et al., 2012). The flux of aragonite and HMC suggests that

supply in the late transgression (Interval 2) was predominantly from the mesophotic zone. The euphotic area on the SMB reached its apex at the end of the transgression (Figure 11A). Monsoonal intensity was close to its peak (between 8 and 6 kyr, de Menocal, 2015), corresponding to the apexes of Mediterranean sapropel S1 (Zirks et al., 2019). This intensification was driven by planetary insolation and corresponds to stronger winds and evaporation in the tropics (Zhao et al., 2005) with maximum expansion of the ITCZ and monsoonal extension (van der Lubbe et al., 2021; Ziegler et al., 2010). These climate changes should correspond to maximum intensity of the western Indian Ocean jet system and upwelling systems (Murtugudde et al., 2007; Prell, 1984; Prell & Van Campo, 1986).

With the initiation of the highstand (Interval 1), sea level nearly reached its current level (Spratt & Lisiecki, 2015). With this high sea-level state, most of the SMB became mesophotic (Figure 11A). The rapid increase in sea level (Figure 11B) likely exceeded the vertical growth rate the reefs established following the transgression (Betzler et al., 2023). Limited pre-existing topography elevated to modern euphotic depth meant that reefs and other build-ups established on the deep substrate could not keep up. It is unclear if additional factors, such as upwelling or turbidity, were at play during this critical time. If they were, it is possible they would also suppress the growth rate resulting in limited keep up over larger regions. As aragonite content in core GC59 diminishes in the highstand (Figure 7C), the Sr/Ca ratio does not (Figure 8G), suggesting that the decline was mainly in LSA from pelagic sources. The lightness value of core GC59 decreases during this period, indicating an overall decline in the carbonate content, also visible to a lesser extent in the two other cores (Figures 9F and 10F). Dust indicators also diminish (Figure 8A). Dilution by organic matter, which would correspond to some increase in nutrients, would explain the shift in lightness value. Likely, there also was a shift in the mode of aragonite supply as the Sr/Ca ratio decreased at the head of the slope (Figure 9E) and increased in the canyon (Figure 10E), possibly due to diminishing aragonite in the fine fraction. This change may indicate more reworking of material from the canyon walls at this time or possibly localised transport of reworked material from the platform itself due to a change in the current bottom regime, intensity or interactions with internal waves. The combined effect would suggest a reduction in more recent sediment supply from the platform at that time. This decrease may have several reasons, including diminishing production with the transition to mesophotic communities, the weakening of storms in the aftermath of the AHP, reduced interaction with the SEC at depth or other some shift in nutrient inputs.

5.4 | Controls and implications

The western Indian Ocean has seen fundamental shifts in its oceanographic controls over geological time scales, governed by climate and atmospheric configuration (Betzler et al., 2016; Bialik, Auer, et al., 2020; Gurlan et al., 2008). Within the Pleistocene to Holocene, atmospheric, oceanic and sea-level changes have had a fundamental sway. Their influence is most notably reflected in the export and distribution patterns of sediment derived from carbonate platforms (Betzler et al., 2013, 2015; Counts et al., 2021; Jorry et al., 2016, 2020; Paul et al., 2012). The complicated relationships among controlling factors are evident in the SMB. In euphotic platforms, downslope supply is dominated by winnowing of the platform top during highstands (Counts et al., 2019; Schlager et al., 1994). The case in the SMB, however, is more complicated with the transition from deeper currents at the base of the platform during the lowstand, increase in focussed supply during the sea-level rise, s.h. the transgression and finally highstand shedding. The significant span of a deeper water region on the SMB allows for persistent euphotic and mesophotic production through the entire glacial cycle, being most abundant in the late transgression rather than during the highstand (Figure 11). The SMB continued to export aragonite despite the significant reduction in the euphotic area with the transition to the highstand, suggesting that dominant factories have shifted along that transition. It is not entirely clear why neritic carbonate production did not keep up with sea level during the transgression.

5.5 | Platform morphology, sea level and drowning

Large differences exist between sediment production and export patterns when comparing the SMB with other large-scale carbonate platforms, for example, the Bahamas (euphotic), the Maldives (mixed euphotic mesophotic) and the GBR (mixed euphotic mesophotic). This difference, to a large extent, depends on a series of interacting factors: (i) the pre-existing morphology that was reflooded during the last glacial–interglacial transition, (ii) the rate of sea-level rise, (iii) the time needed to repopulate the newly flooded carbonate platform areas, (iv) changes in current patterns over time and (v) changing climate conditions (temperature, wind, waves, water turbulence, dust input) associated with the glacial–interglacial transition. Hence, the interaction between the carbonate platform morphology that was reflooded, and all other factors acting at different times ultimately determine the time needed for the carbonate platform to re-establish significant carbonate production again. It is this interplay of various factors that

is expressed in the difference in sediment export pattern when comparing the SMB with the other large-scale carbonate platforms.

The present-day morphology of the SMB, with its deepened margins, differs significantly from the present topographies of the Bahamas, the Maldives and the GBR. The present-day Bahamian carbonate platform is marked by a shallow-water edge surrounding a deeper lagoon with varying water depths (Carew et al., 1997). Numerous inlets connect the inner platform with the surrounding open ocean. The transition from the platform to the slope is at the northern slope of Little Bahama Bank, marked by two pronounced escarpments at 70 and 120 m water depth (Mulder et al., 2017; Rankey & Doolittle, 2012; Tournadour et al., 2017), as for the slope of Tongue of the Ocean (Grammer et al., 1999; Grammer & Ginsburg, 1992) and the western Great Bahama Bank (Rendle & Reijmer, 2002; Wilber et al., 1990) a 3–10° slope connects the shallow-water platform margin with a slope break at 55–65 m, succeeded by a steep cliff down to 140–180 m water depth.

In the Maldives, a similar platform edge to slope morphology is present. The inner platform is significantly deeper reaching water depths of 90 m marking the typical atoll shape (Betzler et al., 2015; Gischler, 2006). A series of submarine terraces are present between 55 and 122 m water depth at North Ari (Fürstenau et al., 2010). In multiple atolls in the Maldives, terraces with varying lateral extensions have been identified between 33 and 106.5 m water depth (Rovere et al., 2018), with a distinct slope break at *ca* 120 m water depth. It is important to note that such terraces do not represent a clear global signal. A comparison with other submerged reef terraces from various locations across the globe (Rovere et al., 2018, their fig. 9) reveal that there is no consistent global pattern because of uncertainties regarding the impact of tectonic processes and glacio-hydro isostatic adjustments.

For the GBR shelf edge, Ribbon Reef offers a good case study. The outer shelf connected to the continental slope extends to a steep shelf break between about 70 and 100 m water depth (Abbey et al., 2011; Puga-Bernabéu et al., 2011). At this shelf-break, the slope gradient changes from <5° to >20°. At the southern Noggin region (Abbey et al., 2011; Puga-Bernabéu et al., 2013), the shelf-break is positioned at 102–109 m water depth. The <1000 to 7000 m wide upper slope is gently inclined (<2.5°) and transfers to about a 9° inclined upper slope at 250–300 m water depth.

Hence, the overall platform edge morphology profiles for the Bahamas, the Maldives and the GBR all demonstrate a large variety when compared to the SMB, and thus other factors must have played a role why the Bahamas, the Maldives and the GBR still have a significant active light (photozoan)-dominated carbonate platform. Such settings are manifested by reef communities with corals,

red algae, green algae, sponges, microbial mats, benthic foraminifera, echinoderms and non-skeletal components, for example, pellets and ooids, although the latter have a clear microbial aspect dominating their growth. Similar reef communities are present at the Maldives and GBR.

The SMB, however, displays a mesophotic assemblage (Betzler et al., 2021, 2023; Lindhorst et al., 2019) as the platform apparently failed to catch up with rising sea level. Hence, no photozoan assembly was established that could catch up with the sea-level rise to reach the euphotic zone. Such an assemblage can be forced by multiple factors including depth, turbidity and nutrients to name a few, which govern the mode of metabolic energy availability (Bialik et al., 2023). Moreover, a certain lag-time exists between the re-flooding of the platform and the renewed start-up of carbonate production, as also demonstrated by differences in the timing of changes in the oxygen stable isotope curve and fluctuations in carbonate sediment production during the glacial–interglacial transition as the community becomes re-established (Emmermann et al., 1999; Sepulcre et al., 2017). The variable probability function of larval dispersal in the western Indian Ocean may farther play into this lag in this region (Vogt-Vincent et al., 2023).

That the SMB displays a different response to the last glacial–interglacial transition might be because sea-level pulses in the Indian Ocean (Camoïn et al., 2004; Zinke et al., 2003) during the transgression did not match with the availability of platform surfaces within the euphotic zone that could be repopulated. A similar scenario was discussed for the southernmost reefs in the Pacific (Lord Howe Island and Balls Pyramid in the Tasman Sea) in which the antecedent topography was the essential parameter (Woodroffe et al., 2023). It was suggested that the maximum growth rate of a euphotic reef is around 12.5 mm/year (Bosscher & Schlager, 1992), the maximum rate of sea-level rise during the Holocene transgression in the region may have been around 19 mm/year between 11.6 and 9.6 kyr cal BP (Camoïn et al., 2004; Zinke et al., 2003), strongly suggesting accumulation could not have kept up. Global compilations (Spratt & Lisiecki, 2016) also suggest periods (notably between 12 and *ca* 14.5 kyr) where the rate of sea-level rise exceeded 15 mm/year. Yet here this is a period marked by high export of neritic material (Figures 8, 9 and 10). Other factors, besides the availability of a suitable settling surface, must therefore be invoked to explain this situation such as lower growth rate, either due to temperature or nutrient state.

The failure to catch up with the rise in sea level together with antecedent topography (Woodroffe et al., 2023), and environmental changes (e.g. increased current activity, changing water masses, influx of nutrients; Bialik et al., 2021; James et al., 2023; Vale et al., 2022) ultimately

obstructed the renewed start of photozoan (euphotic) carbonate production yet, still allowed the start-up of the mesophotic carbonate factory. For euphotic carbonate platforms, the role of wind and nutrients have been also invoked to modulate neritic production (Reijmer & Andresen, 2007; Turpin et al., 2011). It is, therefore, possible that some of the glacial/interglacial variations observed here at the SMB are also the product of the re-organisation of the winds and nutrient regime in the area with post-glacial warming affecting nutrient limitations.

6 | CONCLUSIONS

The Mascarene Plateau is a mostly drowned mesophotic carbonate platform situated in the tropical zone. As such, its response to sea-level changes is somewhat different from that of other carbonate platforms. Material is driven and sloughed from the platform through a combination of storm events, bottom currents and internal waves. These processes induce both the resuspension of fine material in distributed flow and confined grain flows. Material transport from the platform was preferentially confined during the lowstand associated with the LGM and became unconfined towards the end of the Holocene sea-level rise. With the transition to the modern highstand, the supply diminished. The diminishing sediment supply likely led to erosion of the canyon walls due to sediment starvation. The water depth of the platform likely plays a role in the specific transport mechanism through the mode of material production on the platform, depth of internal wave interface, storm wave base depth relative to platform depth and bottom current configuration.

ACKNOWLEDGEMENTS

We acknowledge outstanding support by the Master and crew of *RV SONNE* and by the shipboard scientific party. The research cruise SO270 and post-cruise work was funded by the Bundesministerium für Bildung und Forschung (BMBF, Germany; grant 03G0270A to CB). The Joint Commission of the Extended Continental Shelf Mascarene Plateau Region is thanked for allowing work in the Mascarene Joint Management Area (JMA) and the Department for Continental Shelf, Maritime Zones Administration & Exploration (Mauritius) for allowing work in the EEZ of the Republic of Mauritius. Ilona Schutter (UHH) is thanked for her work within the project and Jutta Richarz (UHH) for grain-size analyses. OMB was supported by Marie Skłodowska Curie fellowship 101003394 (RhodoMalta) during post-cruise work. JR was supported by Ministerio de Ciencia e Innovación of the Spanish Government through the Ramón y Cajal project RYC2021-034362-I. JR and JCB thanks research group

RNM-190. The authors would like to thank the editors as well as two anonymous reviewers.

CONFLICT OF INTEREST STATEMENT

There are no competing financial interests or conflicts of interest. All funding sources for this research are stated in the acknowledgements.

DATA AVAILABILITY STATEMENT

All data and supplements are available online via the FigShare repository as [10.6084/m9.figshare.20000396.v1](https://doi.org/10.6084/m9.figshare.20000396.v1) and available prior to publication through: <https://figshare.com/s/cdaf396b545a38bd0e55>.

ORCID

Or M. Bialik  <https://orcid.org/0000-0003-1915-7297>

John J. G. Reijmer  <https://orcid.org/0000-0001-5807-1256>

REFERENCES

- Abbey, E., Webster, J.M. & Beaman, R.J. (2011) Geomorphology of submerged reefs on the shelf edge of the Great Barrier Reef: the influence of oscillating Pleistocene sea-levels. *Marine Geology*, 288(1–4), 61–78. <https://doi.org/10.1016/j.margeo.2011.08.006>
- Abram, N.J., Hargreaves, J.A., Wright, N.M., Thirumalai, K., Ummenhofer, C.C. & England, M.H. (2020) Palaeoclimate perspectives on the Indian Ocean Dipole. *Quaternary Science Reviews*, 237, 106302. <https://doi.org/10.1016/j.quascirev.2020.106302>
- Alonso-Garcia, M., Reolid, J., Jimenez-Espejo, F.J., Bialik, O.M., Alvarez Zarikian, C.A., Laya, J.C., Carrasquiera, I., Jovane, L., Reijmer, J.J.G., Eberli, G.P. & Betzler, C. (2024) Sea-level and monsoonal control on the Maldives carbonate platform (Indian Ocean) over the last 1.3 million years. *Climate of the Past*, 20(3), 547–571. <https://doi.org/10.5194/cp-20-547-2024>
- Amado-Filho, G.M., Moura, R.L., Bastos, A.C., Salgado, L.T., Sumida, P.Y., Guth, A.Z., Francini-Filho, R.B., Pereira-Filho, G.H., Abrantes, D.P., Brasileiro, P.S., Bahia, R.G., Leal, R.N., Kaufman, L., Kleypas, J.A., Farina, M. & Thompson, F.L. (2012) Rhodolith beds are major CaCO₃ bio-factories in the tropical South West Atlantic. *PLoS One*, 7(4), e35171. <https://doi.org/10.1371/journal.pone.0035171>
- Amante, C. & Eakins, B.W. (2009) ETOPO1 arc-minute global relief model: procedures, data sources and analysis. Boulder, CO.
- Bemis, B.E., Spero, H.J., Lea, D.W. & Bijma, J. (2000) Temperature influence on the carbon isotopic composition of Globigerina bulloides and Orbulina universa (planktonic foraminifera). *Marine Micropaleontology*, 38(3–4), 213–228. [https://doi.org/10.1016/S0377-8398\(00\)00006-2](https://doi.org/10.1016/S0377-8398(00)00006-2)
- Benayahu, Y., Bridge, T.C.L., Colin, P.L., Liberman, R., McFadden, C.S., Pizarro, O., Schleyer, M.H., Shoham, E., Reijnen, B.T., Weis, M. & Tanaka, J. (2019) Octocorals of the Indo-Pacific. In: Loya, Y., Puglise, K. & Bridge, T. (Eds.) *Mesophotic coral ecosystems. Coral reefs of the world*, Vol. 12. Switzerland: Springer, pp. 709–728. https://doi.org/10.1007/978-3-319-92735-0_38
- Betzler, C., Eberli, G.P., Alvarez Zarikian, C.A., Alonso-Garcia, M., Bialik, O.M., Blättler, C.L., Guo, J.A., Haffen, S., Horozal, S.,

- Inoue, M., Jovane, L., Kroon, D., Lanci, L., Laya, J.C., Ling Hui Mee, A., Lüdmann, T., Nakakuni, M., Nath, B.N., Niino, K., Petruny, L.M., Pratiwi, S.D., Reijmer, J.J.G., Reolid, J., Slagle, A.L., Sloss, C.R., Su, X., Swart, P.K., Wright, J.D., Yao, Z. & Young, J.R. (2017) Site U1467. *Proceedings of the International Ocean Discovery Program*, 359(May). <https://doi.org/10.14379/iodp.proc.359.105.2017>
- Betzler, C., Hübscher, C., Lindhorst, S., Lüdmann, T., Reijmer, J.J.G. & Braga, J. (2016) Lowstand wedges in carbonate platform slopes (Quaternary, Maldives, Indian Ocean). *The Depositional Record*, 2(2), 196–207. <https://doi.org/10.1002/dep2.21>
- Betzler, C., Eberli, G.P., Kroon, D., Wright, J.D., Swart, P.K., Nath, B.N., Alvarez-Zarikian, C.A., Alonso-García, M., Bialik, O.M., Blättler, C.L., Guo, J.A., Haffen, S., Horozal, S., Inoue, M., Jovane, L., Lanci, L., Laya, J.C., Mee, A.L.H., Lüdmann, T., Nakakuni, M., Niino, K., Petruny, L.M., Pratiwi, S.D., Reijmer, J.J.G., Reolid, J., Slagle, A.L., Sloss, C.R., Su, X., Yao, Z. & Young, J.R. (2016) The abrupt onset of the modern South Asian Monsoon winds. *Scientific Reports*, 6(1), 29838. <https://doi.org/10.1038/srep29838>
- Betzler, C., Lindhorst, S., Lüdmann, T., Reijmer, J.J., Braga, J.-C., Bialik, O.M., Reolid, J., Eisermann, J.O., Emeis, K., Rixen, T. & Bissessur, D. (2021) Current and sea level control the demise of shallow carbonate production on a tropical bank (Saya de Malha Bank, Indian Ocean). *Geology*, 49(12), 1431–1435. <https://doi.org/10.1130/G49090.1>
- Betzler, C., Lindhorst, S., Lüdmann, T., Weiss, B., Wunsch, M. & Braga, J.C. (2015) The leaking bucket of a Maldives atoll: implications for the understanding of carbonate platform drowning. *Marine Geology*, 366, 16–33. <https://doi.org/10.1016/j.margeo.2015.04.009>
- Betzler, C., Lindhorst, S., Reijmer, J.J.G., Braga, J.C., Lüdmann, T., Bialik, O.M., Reolid, J., Geßner, A., Hainbucher, D. & Bissessur, D. (2023) Carbonate platform drowning caught in the act: the sedimentology of Saya de Malha Bank (Indian Ocean). *Sedimentology*, 70(1), 78–99. <https://doi.org/10.1111/sed.13032>
- Betzler, C., Lüdmann, T., Hübscher, C. & Fürstenau, J. (2013) Current and sea-level signals in periplatform ooze (Neogene, Maldives, Indian Ocean). *Sedimentary Geology*, 290, 126–137. <https://doi.org/10.1016/j.sedgeo.2013.03.011>
- Bialik, O.M., Reolid, J., Betzler, C., Eberli, G.P. & Waldmann, N.D. (2020) Source shifts to periplatform deposits during the early to middle Miocene in response to climatic and oceanographic forcing, Maldives, western Indian Ocean. *Palaeogeography, Palaeoclimatology, Palaeoecology*, 559, 109969. <https://doi.org/10.1016/j.palaeo.2020.109969>
- Bialik, O.M., Auer, G., Ogawa, N.O., Kroon, D., Waldmann, N.D. & Ohkouchi, N. (2020) Monsoons, upwelling, and the deoxygenation of the Northwestern Indian Ocean in response to Middle to Late Miocene global climatic shifts. *Paleoceanography and Paleoclimatology*, 35(2), 1–17. <https://doi.org/10.1029/2019PA003762>
- Bialik, O.M., Bookman, R., Elyashiv, H., Marietou, A., Saar, R., Rivlin, T., Taha, N., Benaltabet, T., Lotem, N., Funaro, E. & Antler, G. (2022) Tropical storm-induced disturbance of deep-water porewater profiles, Gulf of Aqaba. *Marine Geology*, 453, 106926. <https://doi.org/10.1016/j.margeo.2022.106926>
- Bialik, O.M., Coletti, G., Mariani, L., Commissario, L., Desbiolles, F. & Meroni, A.N. (2023) Availability and type of energy regulate the global distribution of neritic carbonates. *Scientific Reports*, 13(1), 19687. <https://doi.org/10.1038/s41598-023-47029-4>
- Bialik, O.M., Varzi, A.J., Duran Gallego, R., Le Bas, T.P., Gauci, A., Micallef, A. & Savini, A. (2021) Mesophotic depth biogenic accumulations (“biogenic mounds”) offshore the Maltese Islands, central Mediterranean Sea. *EarthArxiv* <https://doi.org/10.31223/X5PP8J>
- Blott, S.J. & Pye, K. (2001) GRADISTAT: a grain size distribution and statistics package for the analysis of unconsolidated sediments. *Earth Surface Processes and Landforms*, 26(11), 1237–1248. <https://doi.org/10.1002/esp.261>
- Boardman, M.R., Neumann, A.C., Baker, P.A., Dulin, L.A., Kenter, R.J., Hunter, G.E. & Kiefer, K.B. (1986) Banktop responses to Quaternary fluctuations in sea level recorded in periplatform sediments. *Geology*, 14(1), 28–31. [https://doi.org/10.1130/0091-7613\(1986\)14<28:BRTQFI>2.0.CO;2](https://doi.org/10.1130/0091-7613(1986)14<28:BRTQFI>2.0.CO;2)
- Bosscher, H. & Schlager, W. (1992) Computer simulation of reef growth. *Sedimentology*, 39(3), 503–512. <https://doi.org/10.1111/j.1365-3091.1992.tb02130.x>
- Budd, D.A. & Hiatt, E.E. (1993) Mineralogical stabilization of high-magnesium calcite: geochemical evidence for intracrystal recrystallization within holocene porcellaneous foraminifera. *Journal of Sedimentary Research*, 63(2), 261–274. <https://doi.org/10.1306/D4267AD7-2B26-11D7-8648000102C1865D>
- Caley, T., Malaizé, B., Zaragosi, S., Rossignol, L., Bourget, J., Eynaud, F., Martinez, P., Giraudeau, J., Charlier, K. & Ellouzi-Zimmermann, N. (2011) New Arabian Sea records help decipher orbital timing of Indo-Asian monsoon. *Earth and Planetary Science Letters*, 308(3–4), 433–444. <https://doi.org/10.1016/j.epsl.2011.06.019>
- Camoin, G.F., Montaggioni, L.F. & Braithwaite, C.J.R. (2004) Late glacial to post glacial sea levels in the Western Indian Ocean. *Marine Geology*, 206(1–4), 119–146. <https://doi.org/10.1016/j.margeo.2004.02.003>
- Carew, J.L., Mylroie, J.E., Vacher, H.L. & Quinn, T.M. (1997) Geology of The Bahamas. In: Vacher, L.H.L. & Quinn, T.M. (Eds.) *Geology and hydrogeology of carbonate islands*. Amsterdam, the Netherlands: Elsevier Science, pp. 91–139, Developments in Sedimentology, Vol. 54.
- Counts, J.W., Jorry, S.J., Vazquez-Riveiros, N., Amy, L.A., Dennielou, E. & Jouet, G. (2021) Sedimentology and distribution of late quaternary calciturbidites and calcidebrites in the Mozambique Channel (Southwest Indian Ocean). *Facies*, 67(2), 17. <https://doi.org/10.1007/s10347-021-00624-1>
- Counts, J.W., Jorry, S.J., Vazquez Riveiros, N., Jouet, G., Giraudeau, J., Cheron, S., Boissier, A. & Miramontes, E. (2019) A Late Quaternary record of highstand shedding from an isolated carbonate platform (Juan de Nova, southern Indian Ocean). *The Depositional Record*, 5(3), 540–557. <https://doi.org/10.1002/dep2.57>
- de Menocal, P.B. (2015) End of the African humid period. *Nature Geoscience*, 8(2), 86–87. <https://doi.org/10.1038/ngeo2355>
- Dix, G.R. & Mullins, H.T. (1988a) A regional perspective of shallow-burial diagenesis of deep-water periplatform carbonates from the northern Bahamas. Proc., Scientific Results, ODP, Leg 101, Bahamas, 101, 279–302. <https://doi.org/10.2973/odp.proc.sr.101.132.1988>
- Dix, G.R. & Mullins, H.T. (1988b) Rapid burial diagenesis of deep-water carbonates: Exuma Sound, Bahamas. *Geology*, 16(8), 680. [https://doi.org/10.1130/0091-7613\(1988\)016<0680:RBDODW>2.3.CO;2](https://doi.org/10.1130/0091-7613(1988)016<0680:RBDODW>2.3.CO;2)

- Droxler, A.W., Schlager, W. & Whallon, C.C. (1983) Quaternary aragonite cycles and oxygen-isotope record in Bahamian carbonate ooze. *Geology*, 11(4), 235. [https://doi.org/10.1130/0091-7613\(1983\)11<235:QACAOR>2.0.CO;2](https://doi.org/10.1130/0091-7613(1983)11<235:QACAOR>2.0.CO;2)
- Dunbar, G.B. & Dickens, G.R. (2003) Late Quaternary shedding of shallow-marine carbonate along a tropical mixed siliciclastic-carbonate shelf: Great Barrier Reef, Australia. *Sedimentology*, 50(6), 1061–1077. <https://doi.org/10.1046/j.1365-3091.2003.00593.x>
- Duncan, R.A. & Hargraves, R.B. (1990) $^{40}\text{Ar}/^{39}\text{Ar}$ geochronology of basement rocks from the Mascarene Plateau, the Chagos Bank, and the Maldives Ridge. Proc., Scientific Results, ODP, Leg 115, Mascarene Plateau, 115, 43–51. <https://doi.org/10.2973/odp.proc.sr.115.141.1991>
- Dunham, R.J. (1962) Classification of carbonate rocks according to depositional textures. In: Ham, W.E. (Ed.) *Classification of carbonate rocks—a symposium*. Tulsa: AAPG Memoir 1, pp. 108–121.
- Eberli, G.P., Swart, P.K. & Malone, M.J. (1997) Site 1006. Proceedings of the Ocean Drilling Program, Initial Reports Vol. 166(03), 161–165.
- Emmermann, P. (2000) Mineralogy, geochemistry and microfacies of late Quaternary periplatform sediments: carbonate export cycles and secondary processes—Sanganeb Atoll and Abington Reef, Sudan, Central Red Sea, Christian-Albrechts-Universität Kiel.
- Emmermann, P.P., Reijmer, J.J.G. & Andresen, N. (1999) Sedimentation rates of Late Quaternary periplatform sediments based on aragonite/calcite ratios: Sudanese Red Sea vs. Pedro Bank (Caribbean). In: Bruns, P. & Hass, H.C. (Eds.) *On the determination of sediment accumulation rates*, *GeoResearch Forum* 5. Switzerland: Trans Tech Publications, pp. 67–86.
- Fantle, M.S. & DePaolo, D.J. (2007) Ca isotopes in carbonate sediment and pore fluid from ODP Site 807A: the $\text{Ca}^{2+}(\text{aq})$ -calcite equilibrium fractionation factor and calcite recrystallization rates in Pleistocene sediments. *Geochimica et Cosmochimica Acta*, 71(10), 2524–2546. <https://doi.org/10.1016/j.gca.2007.03.006>
- Fedorov, V.V., Rubinshteyn, I.G., Danilov, I.V. & Ianin, V.I. (1980) Bottom landscape of the Saya de Malha bank in the Indian Ocean. *Oceanology*, 20(4), 434–439.
- Fisher, R.L., Johnson, G.L. & Cheezen, B.C. (1967) Mascarene Plateau, Western Indian Ocean. *GSA Bulletin*, 78(10), 1247–1266. [https://doi.org/10.1130/0016-7606\(1967\)78\[1247:MPWIO\]2.0.CO;2](https://doi.org/10.1130/0016-7606(1967)78[1247:MPWIO]2.0.CO;2)
- Folk, R.L. & Ward, W.C. (1957) Brazos River bar [Texas]: a study in the significance of grain size parameters. *Journal of Sedimentary Research*, 27(1), 3–26. <https://doi.org/10.1306/74D70646-2B21-11D7-8648000102C1865D>
- Fürstenau, J., Lindhorst, S., Betzler, C. & Hübscher, C. (2010) Submerged reef terraces of the Maldives (Indian Ocean). *Geo-Marine Letters*, 30(5), 511–515. <https://doi.org/10.1007/s00367-009-0174-2>
- Gischler, E. (2006) Sedimentation on Rasdhoo and Ari Atolls, Maldives, Indian ocean. *Facies*, 52(3), 341–360. <https://doi.org/10.1007/s10347-005-0031-3>
- Gischler, E. & Zingeler, D. (2002) The origin of carbonate mud in isolated carbonate platforms of Belize, Central America. *International Journal of Earth Sciences*, 91(6), 1054–1070. <https://doi.org/10.1007/s00531-002-0288-5>
- Gourlan, A.T., Meynadier, L. & Allègre, C.J. (2008) Tectonically driven changes in the Indian Ocean circulation over the last 25 Ma: neodymium isotope evidence. *Earth and Planetary Science Letters*, 267(1–2), 353–364. <https://doi.org/10.1016/j.epsl.2007.11.054>
- Grammer, G.M., Crescini, C.M., McNeill, D.F. & Taylor, L.H. (1999) Quantifying rates of syndepositional marine cementation in deeper platform environments—new insight into a fundamental process. *Journal of Sedimentary Research*, 69(1), 202–207. <https://doi.org/10.2110/jsr.69.202>
- Grammer, G.M. & Ginsburg, R.N. (1992) Highstand versus lowstand deposition on carbonate platform margins: insight from Quaternary foreslopes in The Bahamas. *Marine Geology*, 103(1–3), 125–136. [https://doi.org/10.1016/0025-3227\(92\)90012-7](https://doi.org/10.1016/0025-3227(92)90012-7)
- Grossowicz, M. & Benayahu, Y. (2015) Occurrence and survivorship of azooxanthellate octocorals reflect recruitment preferences and depth distribution. *Hydrobiologia*, 759(1), 85–93. <https://doi.org/10.1007/s10750-015-2270-9>
- Heaton, T.J., Köhler, P., Butzin, M., Bard, E., Reimer, R.W., Austin, W.E.N., Bronk Ramsey, C., Grootes, P.M., Hughen, K.A., Kromer, B., Reimer, P.J., Adkins, J., Burke, A., Cook, M.S., Olsen, J. & Skinner, L.C. (2020) Marine20—the marine radiocarbon age calibration curve (0–55,000 cal BP). *Radiocarbon*, 62(4), 779–820. <https://doi.org/10.1017/RDC.2020.68>
- Hubbard, C.R. & Snyder, R.L. (1988) RIR - Measurement and Use in Quantitative XRD. *Powder Diffraction*, 3, 74–77. <https://doi.org/10.1017/S0885715600013257>
- James, N., Blasco, S. & Tucker, T. (2023) Holocene, mesophotic, carbonate sedimentation, Bermuda atoll margin: a submersible study. *Marine Geology*, 460, 107049. <https://doi.org/10.1016/j.margeo.2023.107049>
- Jorry, S.J., Camoin, G.F., Jouet, G., Le Roy, P., Vella, C., Courgeon, S., Prat, S., Fontanier, C., Paumard, V., Boule, J., Caline, B. & Borgomano, J. (2016) Modern sediments and Pleistocene reefs from isolated carbonate platforms (Iles Eparses, SW Indian Ocean): a preliminary study. *Acta Oecologica*, 72, 129–143. <https://doi.org/10.1016/j.actao.2015.10.014>
- Jorry, S.J., Jouet, G., Edinger, E.N., Toucanne, S., Counts, J.W., Miramontes, E., Courgeon, S., Vázquez, N., Le, P. & Camoin, G.F. (2020) From platform top to adjacent deep sea: new source-to-sink insights into carbonate sediment production and transfer in the SW Indian Ocean (Glorieuses archipelago). *Marine Geology*, 423(January), 106144. <https://doi.org/10.1016/j.margeo.2020.106144>
- Kleypas, J.A. (1997) Modeled estimates of global reef habitat and carbonate production since the Last Glacial Maximum. *Paleoceanography*, 12(4), 533–545. <https://doi.org/10.1029/97PA01134>
- Kok, J.F., Adebisi, A.A., Albani, S., Balkanski, Y., Checa-Garcia, R., Chin, M., Colarco, P.R., Hamilton, D.S., Huang, Y., Ito, A., Klose, M., Li, L., Mahowald, N.M., Miller, R.L., Obiso, V., Pérez García-Pando, C., Rocha-Lima, A. & Wan, J.S. (2021) Contribution of the world's main dust source regions to the global cycle of desert dust. *Atmospheric Chemistry and Physics*, 21(10), 8169–8193. <https://doi.org/10.5194/acp-21-8169-2021>
- Lantzsich, H., Roth, S., Reijmer, J.J.G. & Kinkel, H. (2007) Sea-level related resedimentation processes on the northern slope of Little Bahama Bank (Middle Pleistocene to Holocene). *Sedimentology*, 54(6), 1307–1322. <https://doi.org/10.1111/j.1365-3091.2007.00882.x>
- Léon, J.-F. & Legrand, M. (2003) Mineral dust sources in the surroundings of the north Indian Ocean. *Geophysical Research Letters*, 30(6), 1309. <https://doi.org/10.1029/2002GL016690>

- Lindhorst, S., Appoo, J., Artschwager, M., Bialik, O., Birkicht, M., Bissessur, D., Braga, J.-C., Budke, L., Bunzel, D., Coopen, P., Eberhardt, B., Eggers, D., Eisermann, J.O., El Gareb, F., Emeis, K., Geßner, A.-L., Hüge, F., Knaack-Völker, H., Kornrumpf, N., Lenz, N., Lüdmann, T., Metzke, M., Naderipour, C., Neziraj, G., Reijmer, J., Reolid, J., Reule, N., Rixen, T., Saitz, Y., Schäfer, W., Schutter, I., Siddiqui, C., Sorry, A., Taphorn, B., Vosen, S., Wasilewski, T. & Welsch, A. (2019) Saya de Malha Carbonates, Oceanography and Biogeochemistry (Western Indian Ocean) Cruise No. SO270, 2019-09-06—2019-10-23, Hong Kong (China)—Port Louis (Mauritius). SONNE-Berichte, SO270, Gutachterpanel Forschungsschiffe https://doi.org/10.2312/cr_so270
- Lisiecki, L.E. & Raymo, M.E. (2005) A Pliocene-Pleistocene stack of 57 globally distributed benthic $\delta^{18}\text{O}$ records. *Paleoceanography*, 20(1), 1–17. <https://doi.org/10.1029/2004PA001071>
- Lopez-Gamundi, C., Barnes, B.B., Bakker, A.C., Harris, P.(M.), Eberli, G.P. & Purkis, S.J. (2024) Spatial, seasonal and climatic drivers of suspended sediment atop Great Bahama Bank. *Sedimentology*, 71(3), 769–792. <https://doi.org/10.1111/sed.13151>
- Lopez-Gamundi, C., Dobbelaere, T., Hanert, E., Harris, P.M., Eberli, G. & Purkis, S.J. (2022) Simulating sedimentation on the Great Bahama Bank—sources, sinks and storms. *Sedimentology*, 69(7), 2693–2714. <https://doi.org/10.1111/sed.13020>
- Mavume, A., Rydberg, L., Rouault, M. & Lutjeharms, J. (2010) Climatology and landfall of tropical cyclones in the South-West Indian Ocean. *Western Indian Ocean Journal of Marine Science*, 8(1), 15–36. <https://doi.org/10.4314/wiojms.v8i1.56672>
- Melim, L.A., Westphal, H., Swart, P.K., Eberli, G.P. & Munnecke, A. (2002) Questioning carbonate diagenetic paradigms: evidence from the Neogene of The Bahamas. *Marine Geology*, 185(1–2), 27–53. [https://doi.org/10.1016/S0025-3227\(01\)00289-4](https://doi.org/10.1016/S0025-3227(01)00289-4)
- Meyerhoff, A.A. & Kamen-Kaye, M. (1981) Petroleum prospects of Saya de Malha and Nazareth Banks, Indian Ocean. *AAPG Bulletin*, 65(7), 1344–1347. <https://doi.org/10.1306/03B594AE-16D1-11D7-8645000102C1865D>
- Milliman, J.D., Freile, D., Steinen, R.P. & Wilber, R.J. (1993) Great-Bahama Bank aragonitic muds; mostly inorganically precipitated, mostly exported. *Journal of Sedimentary Research*, 63, 589–595.
- Mulder, T., Joumes, M., Hanquiez, V., Gillet, H., Reijmer, J.J.G., Tournadour, E., Chabaud, L., Principaud, M., Schnyder, J.S.D., Borgomano, J., Fauquembregue, K., Ducassou, E. & Busson, J. (2017) Carbonate slope morphology revealing sediment transfer from bank-to-slope (Little Bahama Bank, Bahamas). *Marine and Petroleum Geology*, 83, 26–34. <https://doi.org/10.1016/j.marpetgeo.2017.03.002>
- Mullins, H.T., Wise, S.W., Gardulski, A.F., Hinchey, E.J., Masters, P.M. & Siegel, D.I. (1985) Shallow subsurface diagenesis of Pleistocene periplatform ooze: northern Bahamas. *Sedimentology*, 32(4), 473–494. <https://doi.org/10.1111/j.1365-3091.1985.tb00465.x>
- Murtugudde, R., Seager, R. & Thoppil, P. (2007) Arabian Sea response to monsoon variations. *Paleoceanography*, 22(4), PA4217. <https://doi.org/10.1029/2007PA001467>
- New, A.L., Stansfield, K., Smythe-Wright, D., Smeed, D.A., Evans, A.J. & Alderson, S.G. (2005) Physical and biochemical aspects of the flow across the Mascarene Plateau in the Indian Ocean. *Philosophical Transactions of the Royal Society A: Mathematical, Physical and Engineering Sciences*, 363(1826), 151–168. <https://doi.org/10.1098/rsta.2004.1484>
- Nohl, T., Jarochovska, E. & Munnecke, A. (2018) Revealing the genesis of limestone-marl alternations: a taphonomic approach. *Palaios*, 34(1), 15–31. <https://doi.org/10.2110/palo.2018.062>
- Nohl, T., Steinbauer, M.J., Sinnesael, M. & Jarochovska, E. (2021) Detecting initial aragonite and calcite variations in limestone-marl alternations. *Sedimentology*, 68(7), 3102–3115. <https://doi.org/10.1111/sed.12885>
- Paul, A., Reijmer, J.J.G., Fürstenau, J., Kinkel, H. & Betzler, C. (2012) Relationship between Late Pleistocene sea-level variations, carbonate platform morphology and aragonite production (Maldives, Indian Ocean). *Sedimentology*, 59(5), 1640–1658. <https://doi.org/10.1111/j.1365-3091.2011.01319.x>
- Perrin, C., Bosence, D. & Rosen, B. (1995) Quantitative approaches to palaeozonation and palaeobathymetry of corals and coralline algae in Cenozoic reefs. *Geological Society, London, Special Publications*, 83(1), 181–229. <https://doi.org/10.1144/GSL.SP.1995.083.01.10>
- Poli, M.S., Meyers, P.A. & Thunell, R.C. (2010) The western North Atlantic record of MIS 13 to 10: changes in primary productivity, organic carbon accumulation and benthic foraminiferal assemblages in sediments from the Blake Outer Ridge (ODP Site 1058). *Palaeogeography, Palaeoclimatology, Palaeoecology*, 295(1–2), 89–101. <https://doi.org/10.1016/j.palaeo.2010.05.018>
- Pratson, L.F., Imran, J., Parker, G., Syvitski, J.P.M. & Hutton, E. (2000) Debris Flows vs turbidity currents: a modeling comparison of their dynamics and deposits. In: Bouma, A.H. & Stone, C.G. (Eds.) *Fine-grained turbidite systems*. American Association of Petroleum Geologists, pp. 57–72. <https://doi.org/10.1306/M72703C6>
- Prell, W.L. (1984) Variation of monsoonal upwelling: a response to changing solar radiation. In: Hansen, J.E. & Takahashi, T. (Eds.) *Climate processes and climate sensitivity, volume 29*. Washington, D.C.: American Geophysical Union, Geophysical Monograph Series, pp. 48–57. <https://doi.org/10.1029/GM029.p0048>
- Prell, W.L. & Van Campo, E. (1986) Coherent response of Arabian Sea upwelling and pollen transport to late Quaternary monsoonal winds. *Nature*, 323(6088), 526–528. <https://doi.org/10.1038/323526a0>
- Puga-Bernabéu, Á., Webster, J.M., Beaman, R.J. & Guilbaud, V. (2011) Morphology and controls on the evolution of a mixed carbonate-siliciclastic submarine canyon system, Great Barrier Reef margin, north-eastern Australia. *Marine Geology*, 289(1–4), 100–116. <https://doi.org/10.1016/j.margeo.2011.09.013>
- Puga-Bernabéu, Á., Webster, J.M., Beaman, R.J. & Guilbaud, V. (2013) Variation in canyon morphology on the Great Barrier Reef margin, north-eastern Australia: the influence of slope and barrier reefs. *Geomorphology*, 191, 35–50. <https://doi.org/10.1016/j.geomorph.2013.03.001>
- Rankey, E.C. & Doolittle, D.F. (2012) Geomorphology of carbonate platform-marginal uppermost slopes: insights from a Holocene analogue, Little Bahama Bank, Bahamas. *Sedimentology*, 59(7), 2146–2171. <https://doi.org/10.1111/j.1365-3091.2012.01338.x>
- Rathbun, M.J. (1911) Reports of the Percy Sladen Trust expedition to the Indian Ocean in 1905, under the leadership of Mr. J. Stanley Gardiner. *Marine Brachyura*, 3(11), 191–261.
- Reijmer, J.J.G. & Andresen, N. (2007) Mineralogy and grain size variations along two carbonate margin-to-basin transects (Pedro Bank, Northern Nicaragua Rise). *Sedimentary Geology*, 198(3–4), 327–350. <https://doi.org/10.1016/j.sedgeo.2007.01.018>

- Reijmer, J.J.G., Schlager, W. & Droxler, A.W. (1988) Site 632: Pliocene-Pleistocene sedimentation cycles in a Bahamian basin. In: *Proceedings of the Ocean Drilling Program, Scientific Results - Part B, vol. 101*. College Station, TX: International Ocean Discovery Program, pp. 213–220.
- Ren, J., Jiang, H., Seidenkrantz, M.-S. & Kuijpers, A. (2009) A diatom-based reconstruction of Early Holocene hydrographic and climatic change in a southwest Greenland fjord. *Marine Micropaleontology*, 70(3–4), 166–176. <https://doi.org/10.1016/j.marmicro.2008.12.003>
- Rendle, R.H. & Reijmer, J.J.G. (2002) Quaternary slope development of the western, leeward margin of the Great Bahama Bank. *Marine Geology*, 185(1–2), 143–164. [https://doi.org/10.1016/S0025-3227\(01\)00294-8](https://doi.org/10.1016/S0025-3227(01)00294-8)
- Rendle, R.H., Reijmer, J.J.G., Kroon, D. & Henderson, G.M. (2000) Mineralogy and sedimentology of the Pleistocene to Holocene on the leeward margin of Great Bahama Bank. *Proceeding of the Ocean Drilling Program, Scientific Results*, 166, 61–76. <https://doi.org/10.2973/odp.proc.sr.166.114.2000>
- Reuning, L., Reijmer, J.J.G. & Mattioli, E. (2006) Aragonite cycles: diagenesis caught in the act. *Sedimentology*, 53(4), 849–866. <https://doi.org/10.1111/j.1365-3091.2006.00799.x>
- Roth, S. & Reijmer, J.J.G. (2004) Holocene Atlantic climate variations deduced from carbonate periplatform sediments (leeward margin, Great Bahama Bank). *Paleoceanography*, 19(1), PA1003. <https://doi.org/10.1029/2003PA000885>
- Roth, S. & Reijmer, J.J.G. (2005) Holocene millennial to centennial carbonate cyclicity recorded in slope sediments of the Great Bahama Bank and its climatic implications. *Sedimentology*, 52(1), 161–181. <https://doi.org/10.1111/j.1365-3091.2004.00684.x>
- Rovere, A., Khanna, P., Bianchi, C.N., Droxler, A.W., Morri, C. & Naar, D.F. (2018) Submerged reef terraces in the Maldivian Archipelago (Indian Ocean). *Geomorphology*, 317, 218–232. <https://doi.org/10.1016/j.geomorph.2018.05.026>
- Schlager, W. (2003) Benthic carbonate factories of the Phanerozoic. *International Journal of Earth Sciences*, 92(4), 445–464. <https://doi.org/10.1007/s00531-003-0327-x>
- Schlager, W., Reijmer, J.J.G. & Droxler, A. (1994) Highstand shedding of carbonate platforms. *Journal of Sedimentary Research*, B64(3), 270–281. <https://doi.org/10.1306/D4267FAA-2B26-11D7-8648000102C1865D>
- Schott, F.A. & McCreary, J.P. (2001) The monsoon circulation of the Indian Ocean. *Progress in Oceanography*, 51(1), 1–123. [https://doi.org/10.1016/S0079-6611\(01\)00083-0](https://doi.org/10.1016/S0079-6611(01)00083-0)
- Sepulcre, S., Durand, N. & Bard, E. (2017) Large ^{14}C age offsets between the fine fraction and coexisting planktonic foraminifera in shallow Caribbean sediments. *Quaternary Geochronology*, 38, 61–74. <https://doi.org/10.1016/j.quageo.2016.12.002>
- Shipboard Scientific Party. (1997) Site 1003. In: Eberli, G.P., Swart, P.K. & Malone, M. (Eds.) *Proceedings of the Ocean Drilling Program, 166 Initial Reports*. College Station, Texas: Ocean Drilling Program, Vol. 166, pp. 71–151. <https://doi.org/10.2973/odp.proc.ir.166.106.1997>
- Sirisha, P., Remya, P.G., Balakrishnan Nair, T.M. & Rao, B.V. (2015) Numerical simulation and observations of very severe cyclone generated surface wave fields in the north Indian Ocean. *Journal of Earth System Science*, 124(8), 1639–1651. <https://doi.org/10.1007/s12040-015-0637-y>
- Slowey, N.C., Wilber, R.J., Haddad, G.A. & Henderson, G.M. (2002) Glacial-to-Holocene sedimentation on the western slope of Great Bahama Bank. *Marine Geology*, 185(1–2), 165–176. [https://doi.org/10.1016/S0025-3227\(01\)00295-X](https://doi.org/10.1016/S0025-3227(01)00295-X)
- Southon, J., Kashgarian, M., Fontugne, M., Metivier, B. & Yim, W.W.-S. (2002) Marine reservoir corrections for the Indian Ocean and Southeast Asia. *Radiocarbon*, 44(1), 167–180. <https://doi.org/10.1017/S0033822200064778>
- Spratt, R.M. & Lisiecki, L.E. (2015) A Late Pleistocene sea level stack. *Climate of the Past Discussions*, 11(4), 3699–3728. <https://doi.org/10.5194/cpd-11-3699-2015>
- Spratt, R.M. & Lisiecki, L.E. (2016) A Late Pleistocene sea level stack. *Climate of the Past*, 12(4), 1079–1092. <https://doi.org/10.5194/cp-12-1079-2016>
- Sulpis, O., Agrawal, P., Wolthers, M., Munhoven, G., Walker, M. & Middelburg, J.J. (2022) Aragonite dissolution protects calcite at the seafloor. *Nature Communications*, 13(1), 1104. <https://doi.org/10.1038/s41467-022-28711-z>
- Sulpis, O., Jeansson, E., Dinauer, A., Lauvset, S.K. & Middelburg, J.J. (2021) Calcium carbonate dissolution patterns in the ocean. *Nature Geoscience*, 14(6), 423–428. <https://doi.org/10.1038/s41561-021-00743-y>
- Swart, P.K. & Guzikowski, M. (1988) Interstitial-water chemistry and diagenesis of periplatform sediments from The Bahamas, ODP Leg 101. Proc., Scientific Results, ODP, Leg 101, Bahamas, 101, 363–380. <https://doi.org/10.2973/odp.proc.sr.101.158.1988>
- Swart, P.K., Mackenzie, G.J., Eberli, G.P., Lüdmann, T. & Betzler, C. (2019) Do drifts deposited adjacent to carbonate platforms record the signal of global carbon isotopic values? *Sedimentology*, 66, 1410–1426. <https://doi.org/10.1111/sed.12580>
- Swart, P.K., Oehlert, A.M., Mackenzie, G.J., Eberli, G.P. & Reijmer, J.J.G. (2014) The fertilization of The Bahamas by Saharan dust: a trigger for carbonate precipitation? *Geology*, 42(8), 671–674. <https://doi.org/10.1130/G35744.1>
- Thirumalai, K., DiNezio, P.N., Tierney, J.E., Puy, M. & Mohtadi, M. (2019) An El Niño mode in the glacial Indian Ocean? *Paleoceanography and Paleoclimatology*, 34(8), 1316–1327. <https://doi.org/10.1029/2019PA003669>
- Tournadour, E., Mulder, T., Borgomano, J., Gillet, H., Chabaud, L., Ducassou, E., Hanquiez, V. & Etienne, S. (2017) Submarine canyon morphologies and evolution in modern carbonate settings: the northern slope of Little Bahama Bank, Bahamas. *Marine Geology*, 391, 76–97. <https://doi.org/10.1016/j.margeo.2017.07.014>
- Travin, V.I. (1968) Science-trade investigations AzCherNIRO in north-west region of Indian Ocean. *VNIRO*, 64, 25.
- Turpin, M., Emmanuel, L., Reijmer, J.J.G. & Renard, M. (2011) Whiting-related sediment export along the Middle Miocene carbonate ramp of Great Bahama Bank. *International Journal of Earth Sciences*, 100(8), 1875–1893. <https://doi.org/10.1007/s00531-010-0627-x>
- Vale, N.F., Braga, J.C., de Moura, R.L., Salgado, L.T., de Moraes, F.C., Karez, C.S., de Carvalho, R.T., Salomon, P.S., Menandro, P.S., Amado-Filho, G.M. & Bastos, A.C. (2022) Distribution, morphology and composition of mesophotic ‘reefs’ on the Amazon Continental Margin. *Marine Geology*, 447, 106779. <https://doi.org/10.1016/j.margeo.2022.106779>
- van der Lubbe, H.J.L., Hall, I.R., Barker, S., Hemming, S.R., Baars, T.F., Starr, A., Just, J., Backeberg, B.C. & Joordens, J.C.A. (2021) Indo-Pacific Walker circulation drove Pleistocene African aridification. *Nature*, 598(7882), 618–623. <https://doi.org/10.1038/s41586-021-03896-3>

- Vogt-Vincent, N.S., Mitarai, S. & Johnson, H.L. (2023) High-frequency variability dominates potential connectivity between remote coral reefs. *Limnology and Oceanography*, 68(12), 2733–2748. <https://doi.org/10.1002/lno.12455>
- Vortsepneva, E. (2008) Saya de Malha Bank – an invisible Island in the Indian Ocean, Moscow, Russia.
- Westervelt, P.J. (1963) Parametric acoustic array. *The Journal of the acoustical society of America*, 35(4), 535–537. <https://doi.org/10.1121/1.1918525>
- Wilber, R.J., Milliman, J.D. & Halley, R.B. (1990) Accumulation of bank-top sediment on the western slope of Great Bahama Bank: rapid progradation of a carbonate megabank. *Geology*, 18(10), 970. [https://doi.org/10.1130/0091-7613\(1990\)018<0970:AObTSO>2.3.CO;2](https://doi.org/10.1130/0091-7613(1990)018<0970:AObTSO>2.3.CO;2)
- Woodroffe, C.D., Linklater, M., Brooke, B.P., Nichol, S.L., Hua, Q. & Kennedy, D.M. (2023) Reef growth and carbonate sedimentation at the southernmost Pacific reefs. *Marine Geology*, 459, 107033. <https://doi.org/10.1016/j.margeo.2023.107033>
- Yesson, C., Taylor, M.L., Tittensor, D.P., Davies, A.J., Guinotte, J., Baco, A., Black, J., Hall-Spencer, J.M. & Rogers, A.D. (2012) Global habitat suitability of cold-water octocorals. *Journal of Biogeography*, 39(7), 1278–1292. <https://doi.org/10.1111/j.1365-2699.2011.02681.x>
- Zhao, Y., Braconnot, P., Marti, O., Harrison, S.P., Hewitt, C., Kitoh, A., Liu, Z., Mikolajewicz, U., Otto-Bliesner, B. & Weber, S.L. (2005) A multi-model analysis of the role of the ocean on the African and Indian monsoon during the mid-Holocene. *Climate Dynamics*, 25(7–8), 777–800. <https://doi.org/10.1007/s00382-005-0075-7>
- Ziegler, M., Tuenter, E. & Lourens, L.J. (2010) The precession phase of the boreal summer monsoon as viewed from the eastern Mediterranean (ODP Site 968). *Quaternary Science Reviews*, 29(11–12), 1481–1490. <https://doi.org/10.1016/j.quascirev.2010.03.011>
- Zinke, J., Reijmer, J.J., Thomassin, B., Dullo, W.-C., Grootes, P. & Erlenkeuser, H. (2003) Postglacial flooding history of Mayotte Lagoon (Comoro Archipelago, southwest Indian Ocean). *Marine Geology*, 194(3–4), 181–196. [https://doi.org/10.1016/S0025-3227\(02\)00705-3](https://doi.org/10.1016/S0025-3227(02)00705-3)
- Zirks, E., Krom, M.D., Zhu, D., Schmiel, G. & Goodman-Tchernov, B.N. (2019) Evidence for the presence of oxygen-depleted Sapropel intermediate water across the Eastern Mediterranean during Sapropel S1. *ACS Earth and Space Chemistry*, 3(10), 2287–2297. <https://doi.org/10.1021/acsearthspacechem.9b00128>

How to cite this article: Bialik, O.M., Betzler, C., Braga, J.C., Reijmer, J.J.G., Reolid, J. & Lindhorst, S. (2024) Changes in mesophotic carbonate-platform export across the end of the last glacial cycle (Saya de Malha Bank, western Indian Ocean). *The Depositional Record*, 10, 374–397. Available from: <https://doi.org/10.1002/dep2.299>